PCCP

View Online
Dynamic Article Links

Cite this: *Phys. Chem. Chem. Phys.*, 2011, **13**, 5078–5098

www.rsc.org/pccp

PAPER

EPR parameters of amino acid radicals in *P. eryngii* versatile peroxidase and its W164Y variant computed at the QM/MM level†

Caterina Bernini,[a] Rebecca Pogni,[a] Francisco J. Ruiz-Dueñas,[b] Angel T. Martínez,[b] Riccardo Basosi[a] and Adalgisa Sinicropi*[a]

Received 13th October 2010, Accepted 22nd November 2010
DOI: 10.1039/c0cp02151b

Quantum mechanics/molecular mechanics (QM/MM) methods, employing density functional theory (DFT), have been used to compute the electron paramagnetic resonance (EPR) parameters of tryptophan and tyrosyl radical intermediates involved in the catalytic cycle of *Pleurotus eryngii* versatile peroxidase (VP) and its W164Y variant, respectively. These radicals have been previously experimentally detected and characterized both in the two-electron and one-electron activated forms of the enzymes. In this work, the well-studied W164 radical in VP has been chosen for calibration purposes because its spectroscopic properties have been extensively studied by multifrequency EPR and ENDOR spectroscopies. Using a B3LYP/CHARMM procedure, appropriately accounting for electrostatic, such as hydrogen bonding, and steric environmental interactions, a good agreement between the calculated and measured EPR parameters for both radicals has been achieved; *g*-tensors, hyperfine coupling constants (hfcc) and Mulliken spin densities have been correlated to changes in geometries, hydrogen bond networks and electrostatic environment, with the aim of understanding the influence of the protein surroundings on EPR properties. In addition, the present calculations demonstrate, for VP, the formation of a neutral tryptophan radical, hydrogen bonded to the nearby E243, *via* a stepwise electron and proton transfer with earlier involvement of a short-lived tryptophan cationic species. Instead, for W164Y, the QM/MM dynamics simulation shows that the tyrosine oxidation proceeds *via* a concerted electron and proton transfer and is accompanied by a significant reorganization of residues and water molecules surrounding the tyrosyl radical.

Introduction

Amino acid radicals have been demonstrated to play an essential role in many enzymatic processes as intermediates in electron, proton or hydrogen atom transfer.[1–3] They have been identified as tyrosyl radicals in aerobic ribonucleotide reductase (RNR)[4–7] and in photosystem II,[8] as tryptophan radicals in DNA photolyase,[9] cytochrome c peroxidase,[10,11] *Escherichia coli* Y177W mutant of RNR[12] and azurin,[13] as cysteine thiyl radicals in a class II RNR from *Lactobacillus leichmannii*[14] and also as glycyl radicals in anaerobic RNR[15–17] and in pyruvate formate lyase.[15]

Due to their open-shell configurations, detection and identification of these catalytically essential redox-active amino acids have been almost exclusively obtained using electron paramagnetic resonance (EPR) spectroscopy and related techniques such as electron-nuclear double-resonance (ENDOR) spectroscopy.

With the aim of a better understanding of tryptophan-mediated electron transfer reactions, most of the experimental work on tryptophan radicals has been focused on the unambiguous assignment of the observed spectral data to a neutral deprotonated or cationic protonated species. This assignment is often difficult due to possible electronic coupling of the radical with other paramagnetic centers or the presence of other radicals. The picture is made even more complicated by the possibility that some observed EPR spectra may actually originate from tyrosyl radicals.

Examples where EPR spectra of tryptophan radicals show signals that are not obscured by any coupling are RNR mutants[18,19] and a Re-labeled azurin.[13] Recently, also another uncoupled tryptophan radical has been directly detected and to a great extent characterized in a class of heme enzymes, that are completely depleted of tyrosines, called versatile peroxidases (VPs).[20–22]

VPs are ligninolytic heme peroxidases produced by fungi from the genera *Pleurotus* and *Bjerkandera*.[23–29]

[a] *Department of Chemistry, University of Siena, Via A. De Gasperi 2, 53100 Siena, Italy. E-mail: sinicropi@unisi.it; Fax: +39 0577 234239; Tel: +39 0577234257*
[b] *Centro de Investigaciones Biológicas, Consejo Superior de, Investigaciones Cientificas, 28040 Madrid, Spain*
† Electronic supplementary information (ESI) available: QM/MM and MD (QM/MM) details, models and tables. See DOI: 10.1039/c0cp02151b

VPs oxidize Mn^{2+}, as do manganese peroxidases (MnPs), as well as high-redox-potential aromatic compounds, such as veratryl alcohol (VA), as do lignin peroxidases (LiPs). VPs are also able to efficiently oxidize different phenolic and low-redox-potential compounds that are the substrates of generic peroxidases (EC 1.11.1.7), such as nonligninolytic peroxidases from the soil basidiomycete *Coprinopsis cinerea* (CiP) or horseradish peroxidase (HRP). Moreover, VPs directly oxidize dyes, including RB5,[23,30,31] polycyclic aromatic hydrocarbons,[32,33] polymeric dyes[34,35] and lignin.[36] The latter is oxidized by LiPs only in the presence of redox mediators.[30,32,34,37] This makes VPs very promising in the biological degradation of large molecules like dyes manufactured by colour industries.[37]

The catalytic activity of VPs resembles the classical heme peroxidase cycle, which involves the formation of Compound I (a two-electron oxidized form, called VPI) after H_2O_2 activation of the resting state. VPI consists of a high-valent iron intermediate (as an oxo-ferryl species) and a porphyrin π-(called VPI_A) or an amino acid (called VPI_B) radical. It undergoes either a self-reduction or a back-reduction by substrates in a two-step reaction that involves the formation of Compound II (a one-electron oxidized form, VPII) followed by closure of the catalytic cycle to the resting state. The VPII activated form of the enzyme involves the equilibrium between $VPII_A$ (an oxo-ferryl species) and $VPII_B$ (containing Fe^{3+} and an amino acid radical).[38]

Previous structural,[39,40] site-directed mutagenesis[41] and spin-trapping[42] studies on LiP proposed that a short-lived surface tryptophan radical (W171) is the oxidation site for VA. However, no direct evidence for the formation of the W171 radical species has been yet reported. Recently, Smith *et al.*[43] engineered the CiP peroxidase to reproduce the catalytic tryptophan site of LiP and manipulated the microenvironment of W171 in LiP with the aim of detecting the tryptophan radical. The resulting variants were characterized by EPR spectroscopy and the involvement of a tryptophan radical intermediate as redox-active cofactor for enzyme catalysis in LiP was demonstrated.

A multifrequency-X-band (9.4 GHz) and W-band (94 GHz)-EPR investigation on a freeze-quenched radical intermediate directly detected in the reaction of *P. eryngii* VP with H_2O_2, combined with ENDOR measurements, unambiguously demonstrated the involvement of a solvent exposed neutral tryptophan radical in the mechanistic catalytic cycle of VP.[20,21] In particular, it has been suggested that the neutral tryptophan radical evolves from a short-lived tryptophan radical cation that is generated from the proposed Fe^{4+}═O porphyrin π-cation radical followed, in a second step, by deprotonation at nitrogen of the pyrrole ring. Additionally, ENDOR data strongly support the presence of a neutral radical H-bonded at the pyrrole nitrogen. The comparison of experimental *g*-tensors, hyperfine coupling constants (hfcc) and McConnell spin densities (ρ) with the results from density functional theory (DFT) calculations on neutral and cationic radical models of tryptophan have further confirmed the presence of a neutral species, N-deprotonated and H-bonded.[21] Here hydrogen bond donor has been simulated using a water molecule and bulk solvent effects have been taken into account by using the polarizable continuum model (PCM).[44] By inspection of the cavity where the tryptophan residue is located in VP, it has been suggested by the authors[20,21] that the most probable hydrogen bond donor is a nearby glutamic acid residue. Furthermore, based on the side chain orientation derived from the experimental isotropic hfcc values for the β-methylene protons, the observed neutral tryptophan radical has been assigned to W164 (excluding the other possible tryptophan residue, W224), which is proposed as the surface site involved in long-range electron transfer (LRET). Low-temperature EPR characterization, combined with steady-state and transient state kinetics, also demonstrated that the tryptophan radical is present in both VPI_B and $VPII_B$ oxidized forms of VP.

In a more recent work,[38] site-directed mutagenesis was used to substitute W164 with a tyrosine residue in VP. The crystallographic analysis of the W164Y variant structure revealed that the main difference between VP and W164Y is the presence of two different conformations of the R257 aliphatic side chain in VP, in contrast to the presence of only one stable conformation of the same residue in W164Y (Fig. 1).

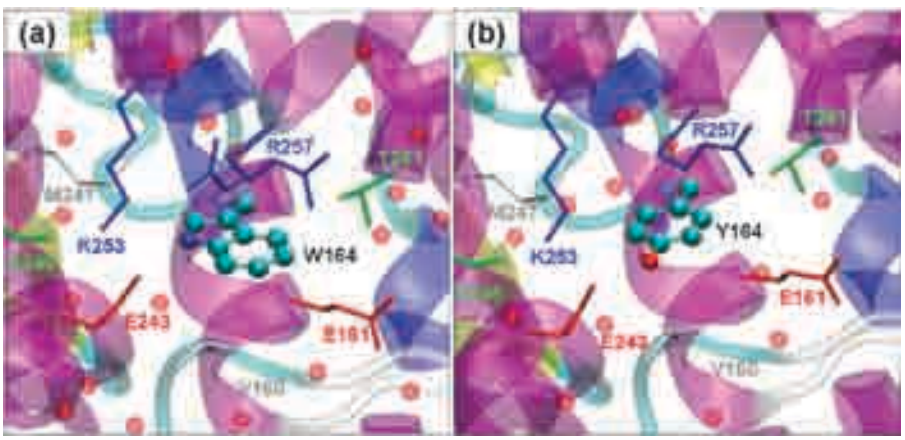

Fig. 1 Comparison of the surface active site environment in (a) VP (pdb code: 2BOQ) and (b) W164Y variant (pdb code: 2W23). A ball-and-stick representation is used for the atoms of W164 and Y164 radical sites. Red dots indicate crystal water molecules. The double conformation of the R257 aliphatic side chain in VP compared to the single conformation of R257 in W164Y is shown.

EPR measurements on the variant revealed the formation of a tyrosyl radical in both VPI_B and $VPII_B$ of W164Y but with lower yields than in native VP. Furthermore, VPII self-reduction is slower in W164Y, as shown by transient-state kinetics and by the absence of the resting state Fe^{3+} in EPR, with the same experimental conditions used for VP. In addition, steady-state kinetics on W164Y showed a reduced activity in oxidizing substrates compared to native VP.[38]

Previous theoretical calculations on tryptophan or tyrosyl radicals have disregarded the effects of the whole protein surrounding and the solvent, or treated them by dielectric continuum approaches, such as PCM.[21,45] Unfortunately, the continuum models do not consider electrostatic (such as hydrogen bonding) and steric interactions that may contribute to the overall stability and electronic properties of the radical species. This is particularly important for the calculations of spectroscopic properties such as EPR magnetic parameters that are strongly influenced by the protein environment. Thus, a more realistic model should include the entire protein together with the surrounding solvent cage.

An all-electron calculation on the entire system is obviously impossible, therefore the method of choice for the description of chemical and spectroscopic processes occurring within very large systems is the hybrid quantum-mechanical/molecular mechanical (QM/MM) method.[46,47] Within this approach, a suitable and reactive part of the system, such as the active site of an enzyme, is treated with accurate QM methods while the environment (the protein matrix and the solvent) is modelled with a lower level of theory such as molecular mechanics (MM) methods.

In recent years, there has been a widespread diffusion of QM/MM calculations of structures, reactivity and spectroscopic properties of proteins and enzymes.[48–66] In fact, this strategy assures that the influence of the protein on the geometry of hydrogen bonds and on the spectroscopic parameters is adequately included in the calculations.

Herein we report a QM/MM and dynamical QM/MM (QM/MM MD) study to characterize the electronic structure of tryptophan and tyrosyl radicals inside the protein matrix of VP and W164Y enzymes and to address the influence of the protein environment on EPR properties of these two radicals. In particular, we correlate *g*-tensors, hfcc and Mulliken spin densities to changes in geometries, hydrogen bond networks and electrostatic environment. Furthermore, the mechanism that leads to the formation of these radical species in terms of concerted or stepwise electron and proton transfer processes is clarified. We also compare the results obtained from our QM/MM calculations including the enzyme environment with previous *in vacuo* or PCM pure quantum mechanical calculations.

To the best of our knowledge, only a few QM/MM studies have so far reported the calculation of spectroscopic properties, such as EPR parameters, of radical species.[53,67–71] Furthermore, this is also the first time that QM/MM calculations have been used to generate EPR data, to characterize the electronic nature of the radical intermediate species and speculate on the protein environment in VP.

Computational details

Setup of the system

Initial structures for VP (pdb code: 2BOQ) and its W164Y variant (pdb code: 2W23) were obtained from the Protein Data Bank (1.33 Å and 1.94 Å resolution, respectively). The results of PROPKA2.0[72] runs were used to assign the protonation states of all titratable residues at the experimental pH (pH = 4.5). The protonated and neutralized systems were solvated in rectangular boxes ($69 \times 80 \times 76$ Å^3 for VP and $75 \times 65 \times 73$ Å^3 for W164Y) of TIP3P water molecules using VMD, version 1.8.6.[73] See the ESI† for further details on the setup.

Force field calculations

CHARMM27 force field[74] and TIP3P water model[75] were used for both pure MM and hybrid QM/MM calculations. All available force field parameters and charges were taken from the CHARMM27 library.[74] For the treatment of the heme, we used the existing CHARMM parameter set for a Fe^{2+} containing heme group,[76] except that the atomic charges were modified to account for the different charge distribution in the Fe^{3+}-porphyrin complex (see the ESI†). The one-electron oxidized form, $VPII_B$, was chosen as model for our computations since both the 2BOQ and 2W23 crystallographic structures have a Fe^{3+} containing heme group. Moreover, we were interested in investigating the self-reduction process of both enzymes that involves the $VPII_B$.

The solvated systems were relaxed by performing classical energy minimization and molecular dynamics (MD) simulations with the NAMD 2.6 code.[77] The positions of the hydrogen atoms and solvent molecules were first energy minimized and then equilibrated at 298 K and 1 atm for 10 ns with a timestep of 1 fs. Electrostatic interactions were taken into account using the Particle Mesh Ewald (PME) method[78] and Periodic Boundary Conditions (PBC) were applied. This run permitted to the solvent to become equilibrated with the solute. A snapshot was extracted at the end of the 10 ns MD runs for both systems, hereafter referred as **fix-(VP_10ns)** and **fix-(W164Y_10ns)**, featuring the same protein backbone and side-chain conformations of the X-ray structures. Further 10 ns equilibration was carried out in which even the protein side-chains were left free to equilibrate. During the MD simulations the coordinates of non-hydrogen atoms of the heme, including the iron-coordinated water molecule, and protein backbone atoms were kept fixed to the crystal structure. Once the systems were equilibrated, five snapshots were separately taken at 200 ps intervals along the last nanosecond of the MD equilibration runs (*i.e.* after 9.2, 9.4, 9.6, 9.8 and 10 ns). These snapshots are hereafter referred as **VP_Xns** and **W164Y_Xns** (X = 9.2, 9.4, 9.6, 9.8, 10). All selected snapshots were energy minimized and then used as starting structures for the following QM/MM and QM/MM MD (only for **W164Y_10ns**) computations.

QM/MM calculations

The QM/MM calculations were performed with the MOLCAS 7.4 package,[79] coupled with a modified version of the MM

package Tinker 4.2.[80] An electronic embedding scheme was applied to include the polarizing effect of the enzyme and solvent environment on the QM region. Hydrogen link atoms[81,82] (HLA) were used at the QM/MM boundary along with the scaled-charge model. QM regions (see **M1** and **M2** in Scheme 1) include tryptophan or tyrosine residue in VP and W164Y, respectively, and the negatively charged glutamate residue (E243). The frontier is placed at the CO–Cα bond of V163, at the Cα–NH bond of L165 and at the Cα–Cβ bond of E243. Further details on the QM/MM methodology and setup are documented in the ESI†.

The QM/MM geometry optimizations were performed using the unrestricted open-shell density functional theory (DFT) with the B3LYP functional[83–85] while CHARMM27 force field[74] was employed for the treatment of the MM part. A mixed basis set (hereafter called 6-31G**#) was used: the 6-31G** basis set for all atoms except the atoms involved in the proton transfer (indolic H1 and N1, phenolic H1 and O1, carboxylic oxygen O2 of E243) for which the 6-311++G** basis set was used. The Morokuma's scheme as implemented in MOLCAS 7.4[79] was applied to constraint the LA position on the line connecting the QM and the MM atoms.

The tryptophan radical in VP enzyme was studied both in its cationic form (**VP_Xns-cat**) and in its neutral form (**VP_Xns-neu**). The resting state (**VP_10ns-RS**), having the tryptophan in its non-radical form, has been also computed. The neutral form was obtained transferring the H1 proton to the O2 oxygen of the carboxylic group of E243. For W164Y variant, two different geometrical frames were analyzed: (1) structures obtained directly from the QM/MM optimization (**W164Y_Xns-A**), featuring the H1 proton completely transferred to the O2 oxygen of E243 and (2) structures obtained from (1) breaking the O1–H2 hydrogen bond and allowing the formation of a new hydrogen bond between H1 and the oxygen of a nearby water molecule (**W164Y_Xns-B**). EPR parameters were computed on the all set of QM/MM optimized geometries.

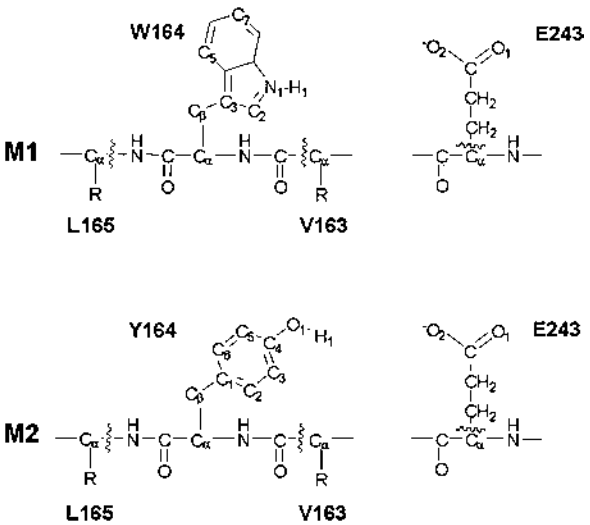

Scheme 1 Definition of the QM regions **M1** and **M2** for QM/MM calculations in VP and W164Y, respectively. The frontier is placed at the CO–Cα bond of V163, the Cα–NH bond of L165 and at the C_α–C_β bond of E243.

QM/MM MD calculations

Dynamical hybrid quantum mechanics/classical mechanics (QM/MM MD) studies were carried out on W164Y using the CP2K software.[86] The QM/MM driver is based on the quantum mechanical program QUICKSTEP[87,88] and the molecular mechanics driver FIST, which are both part of the CP2K package. The general QM/MM scheme, recently developed for large-scale molecular dynamics simulations,[89,90] is based on a multigrid technique for computing the electrostatic potential due to the MM atoms. The quantum region is treated at the DFT level, using the gradient-corrected exchange–correlation functional BLYP,[84] whereas the remaining part of the system is modeled at the classical mechanics level with the CHARMM27 force field.[74] A triple-ξ valence basis set with two sets of polarization function, TZV2P,[91] and an auxiliary plane-wave basis set with a density cutoff of 280 Ry (in a 20 Å cubic box)[63,89,92,93] were used to describe the wavefunction. It has been shown that the high-level basis set is necessary for accurate geometries as well as for energetics.[63,89,92,93] Dual-Space Gaussian (Goedecker–Teter–Hutter) Pseudopotentials[94,95] optimized for the BLYP functional were used for describing core electrons and nuclei. The model **W164Y_10ns** was used as starting geometry for the QM/MM MD simulations. The quantum region is defined as in the previous section.

An MD run within the Born–Oppenheimer approximation was performed on the whole system at 298 K using an NVT ensemble and collecting 1 ps of unconstrained QM/MM dynamics, with an integration time step of 0.5 fs. Only the coordinates of the heme were kept fixed to the X-ray structure. The temperature was kept constant with a Nosé–Hoover thermostat.[96,97] At the end of 1 ps QM/MM MD run, a snapshot was extracted (**W164Y_10ns-cp2k**) for the evaluation of EPR parameters.

Computation of EPR parameters

The spectroscopic EPR data have been computed at the B3LYP/TZVP level of theory‡ using the program package ORCA.[98] The MM point charges are taken into account by the use of the module "orca_pc" which adds the MM point charge contribution to the one-electron matrix and the nuclear repulsion.

Results and discussion

Molecular *g*-tensors, hfcc and Mulliken spin densities for organic radicals can be calculated with high accuracy using DFT methods.[70,99–107] The inclusion of all the electrostatic and steric interactions that may influence the nature and properties of the radical species allows a more direct comparison between computations and experiments. Concerning the present work, a proper modeling of these environmental effects using modern hybrid QM/MM methods

‡ The spectroscopic data have also been obtained from additional single-point calculations at all sets of optimized structures using several hybrid density functionals (B3LYP, PBE0, TPSSh) in combination with the TZVP and EPR-II spectroscopic basis sets for all atoms (see the ESI†).

allows one to: (i) support and complement the experimental results; (ii) determine the electronic and geometric structure of the radical; (iii) evaluate, at a high degree of detail, the interactions that mainly contribute to the overall magnetic properties of free radicals.

In the next sections, we will show the computational feasibility of the QM/MM and QM/MM MD calculations in achieving the above mentioned goals for VP and W164Y enzymes.

1. VP

B3LYP/TZVP parameters computed at the QM/MM optimized geometries of **VP_10ns-neu** and **VP_10ns-cat** radicals (see structures in Fig. 2) are shown in Table 1 (second and third columns) and are compared with experimental values from ref. 20 (first column).

The computed *g*-tensor values (see Scheme 2 for the *g*-tensors orientation), for both neutral and cationic structures, are in very good agreement with the experimental data also considering that the general accepted accuracy for *g*-tensors calculation of organic radicals with DFT methods is within 100–200 ppm of the experimental values.

As previously reported in ref. 20 and 21 the discrimination between W164 neutral and cationic radicals is not possible on the basis of *g*-tensor values only. To this end, it is more useful to inspect the computed Mulliken spin densities that are known to be different between these two species.[108] In fact, the pyrrole ring is significantly affected by the retention or loss of the H1 hydrogen at N1, leading to a quantitatively different spin density on N1 and C3 (see Table 1) , between the neutral and cationic forms, while the spin density distribution on the benzene ring (see C5 and C7 in Table 1) is large and similar for the two species. In addition, spin density on C2 is expected to be larger for the radical cation. Consistent with this picture, our calculated values for the tryptophan radical cation predict a smaller spin density on C3 and N1 and larger and more positive spin density on C2. Moreover and as expected, a larger isotropic hfcc for H1 is computed. These results do not fit the experimental findings and exclude the assignment of the EPR spectra to a radical cation.

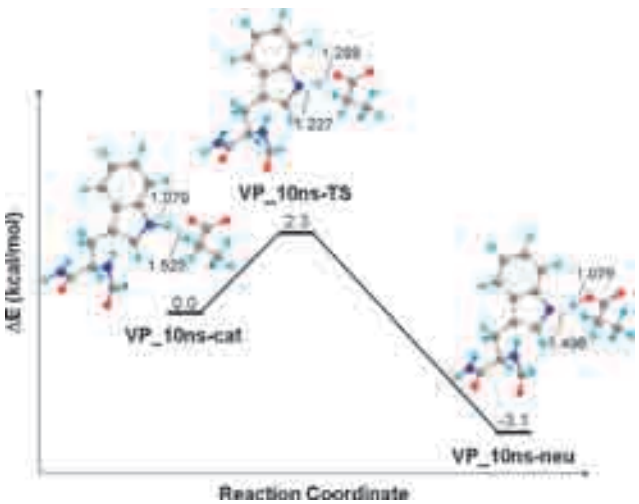

Fig. 2 B3LYP/6-31G**#:CHARMM energy profile for the proton transfer in **VP_10ns** model. The changes of the two main geometrical parameters (N1–H1 and H1–O2 bond lengths given in Å) of tryptophan radical cation (**VP_10ns-cat**), transition state (**VP_10ns-TS**) and neutral tryptophan radical (**VP_10ns-neu**) are shown.

Considering that DFT computed hfcc are generally within ~10–20% of experimental data, our computed parameters, for the neutral species, well reproduce the large (~isotropic) hfcc values for the β-methylene protons, A_i(H-β1) and A_i(H-β2), the anisotropic hfcc for the ring protons, A_i(H-5) and A_i(H-7), and the large anisotropic hfcc for N1, A_i(N1). The deviations from the experimental values of A_i(H-β1) (0.01 mT, which is below the experimental error) and A_i(H-β2) (0.13 mT), which are primarily responsible for the spectrum line shape, are well within the DFT accepted accuracy. The A_i(H-β1) and A_i(H-β2) computed for the radical cation deviate more (~0.30 mT) from the experimental results.

To assess the impact of different enzyme conformations on the electronic structure of the radical, we extracted five snapshots at regular intervals (200 ps) from the last nanosecond of a 10 ns MD equilibration run. Nevertheless, a complete sampling of the configurational space of the system by means of statistical methods, including a correct treatment of the QM part, would have a rather high computational cost. The five geometries were then used as starting points for QM/MM geometry optimizations of both the cationic and the neutral species. The computed parameters for the five snapshots (see Table 1 for **VP_10ns-neu** and Table 2 for **VP_Xns-neu** (X = 9.2, 9.4, 9.6, 9.8)) are very similar, having *g*-tensor values varying within 30 ppm and isotropic hfcc values within ~0.07 mT.

It is important to note that the experimental values are well within these computed ranges. Thus, it appears that considering the suitable environmental interactions, a near-quantitative agreement with measured values can be achieved.

Furthermore, the computed set of *g*-tensors, hfcc data and the Mulliken spin densities definitively confirms the formation of a N-deprotonated neutral tryptophan radical and H-bonded to E243. Besides, the good fit of the computational and experimental data, strongly suggests that the QM/MM computed structure of the neutral tryptophan radical, in its natural environment, is a correct model that allows for a subsequent detailed analysis of such properties that are not experimentally detectable.

The results provided by this study are an improvement over previous calculations on the neutral tryptophan radical model (*N*-deprotonated 3-ethylindole H-bonded with a water molecule, see Trp + H_2O in Table 1) *in vacuo* or considering the bulk solvent effects *via* PCM,[21] especially for the hfcc values for the β-methylene protons H-β1 and H-β2. It is accepted that A_i(H-β1) and A_i(H-β2) are mainly a function of the spatial orientation ϕ defined by the Cα–Cβ–C3–C_2 dihedral angle In previous calculations, this value has been constrained to the X-ray structure value ($\phi \sim -21°$) while in the present work it is obtained relaxing the system in the protein matrix resulting in a slightly different oriented geometry ($\phi \sim -22°$; the complete set of angles and bonds for the optimized geometry is shown in Table 3). This small difference can only partly contribute to the deviation in hfcc

Table 1 B3LYP/TZVP *g*-tensors, hfcc (mT) and Mulliken spin densities computed at different QM/MM optimized geometries of VP tryptophan neutral and cation radicals in comparison with EPR experimental data[a] and results from previous *in vacuo* and PCM[b] calculations

			B3LYP/TZVP//B3LYP/6-31G**#					
		Exp.[a]	VP_10ns-neu	VP_10ns-cat	fix-VP_10ns-neu	fix-VP_10ns-cat	*in vacuo*[b] Trp + H_2O	PCM[b] Trp + H_2O
g-tensors								
g_i	iso	2.00276	2.00286	2.00286	2.00287	2.00285	2.00304	2.00298
	x	2.00352	2.00352	2.00349	2.00353	2.00349	2.00372	2.00357
	y	2.00255	2.00276	2.00273	2.00275	2.00270	2.00291	2.00289
	z	2.00220	2.00232	2.00237	2.00232	2.00236	2.00248	2.00247
hfcc								
A_i(H-β1)	iso	2.60	2.59	2.33	2.62	2.26	2.86	3.14
	x	2.35	2.47	2.22	2.49	2.15	2.73	3.01
	y	2.75	2.78	2.50	2.81	2.43	3.06	3.33
	z	2.70	2.53	2.27	2.56	2.20	2.79	3.08
A_i(H-β2)	iso	1.15	1.01	0.89	0.97	0.83	1.19	1.31
	x	1.13	0.95	0.84	0.90	0.78	1.07	1.19
	y	1.13	0.90	0.78	0.85	0.73	1.12	1.25
	z	1.18	1.19	1.05	1.14	0.98	1.38	1.49
A_i(H1)	iso	0.01	−0.06	−0.35	−0.07	−0.38	0.01	0.01
	x	−0.10	−0.22	−0.65	−0.22	−0.68	−0.08	−0.08
	y	0.19	0.20	0.08	0.20	0.05	0.18	0.17
	z	−0.07	−0.17	−0.49	−0.18	−0.51	−0.06	−0.07
A_i(H2)	iso	0.04	−0.19	−0.34	−0.20	−0.39	0.01	−0.05
	x	0.28	−0.34	−0.45	−0.35	−0.50	0.17	0.14
	y	−0.04	0.07	−0.01	0.07	−0.03	−0.03	−0.12
	z	−0.11	−0.31	−0.57	−0.32	−0.64	−0.13	−0.18
A_i(H-5)	iso	—	−0.51	−0.55	−0.51	−0.55	−0.42	−0.44
	x	−0.64	−0.75	−0.81	−0.75	−0.83	−0.60	−0.63
	y	≤|0.15|	−0.22	−0.23	−0.22	−0.23	−0.18	−0.20
	z	−0.49	−0.57	−0.60	−0.57	−0.61	−0.47	−0.50
A_i(H-7)	iso	—	−0.42	−0.44	−0.41	−0.44	−0.34	−0.36
	x	≤|0.15|	−0.14	−0.14	−0.14	−0.14	−0.10	−0.11
	y	−0.62	−0.66	−0.69	−0.66	−0.70	−0.56	−0.57
	z	−0.46	−0.45	−0.47	−0.45	−0.48	−0.37	−0.39
A_i(N1)	iso	—	0.23	0.19	0.24	0.17	0.31	0.34
	x	≤|0.15|	−0.08	−0.08	−0.08	−0.09	−0.13	−0.07
	y	≤|0.15|	−0.09	−0.10	−0.09	−0.10	−0.12	−0.06
	z	1.00	0.88	0.74	0.88	0.70	1.19	1.15
Spin densities[c]								
N1		0.20	0.19	0.15	0.19	0.14	0.28	0.25
C2		≤|0.05|	0.01	0.08	0.01	0.11	−0.10	−0.04
C3		0.52	0.56	0.48	0.56	0.46	0.61	0.53
C4		—	−0.19	−0.18	−0.19	−0.18	—	—
C5		0.17	0.26	0.27	0.25	0.27	0.22	0.18
C6		—	−0.09	−0.10	−0.09	−0.10	—	—
C7		0.15	0.19	0.19	0.18	0.19	0.16	0.14
C8		—	0.02	0.05	0.02	0.06	—	—
C9		—	0.06	0.04	0.06	0.03	—	—
Cβ		—	−0.03	−0.03	−0.03	−0.02	—	—

[a] Experimental data from ref. 20. The *g*-tensor values are given with a maximum error of ±0.0001. Hfcc (mT) are given with an estimated error of ±0.05 mT. [b] Calculated values from ref. 20 and 21, both *in vacuo* and adding the bulk solvent effects *via* PCM, for a neutral radical model of tryptophan (3-ethylindole) deprotonated at N1, where hydrogen bond donor has been simulated using a water molecule. The structure was optimized *in vacuo* while constraining the Cα–Cβ–C3–C2 dihedral angle to the value (−21.1°) of the X-ray structure (2BOQ). [c] Calculated Mulliken spin densities for nitrogen and carbons of the indolic ring and for Cβ. The total Mulliken spin density is equal to one adding the small contributions from the remaining QM atoms.

values between Trp + H_2O model and the present QM/MM system. The main reason has to be ascribed to a shorter hydrogen bond length in our relaxed QM/MM system (∼1.50 Å) compared to ∼1.98 Å for the Trp + H_2O model system.

Stepwise PCET

Though the involvement of a neutral tryptophan radical as intermediate in the long-range electron transfer process occurring in the reaction of VP with H_2O_2 is now definitively

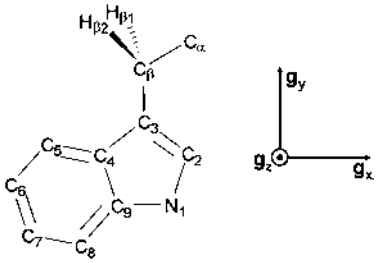

Scheme 2 Tryptophan radical with numbering scheme and *g*-tensor principal axes orientation with respect to the molecular frame: the g_x is in the pyrrole ring, almost parallel to the C9–N1 bond, g_z perpendicular to the ring plane and g_y mutually perpendicular to the other two components.

demonstrated, the mechanism leading to its formation is still unresolved. The earlier involvement of a radical cation (either a porphyrin π- or a tryptophan radical cation) is very likely but it has never been experimentally verified, even using fast freeze-quench experiments with a time resolution of few milliseconds.

In principle, the proton-coupled electron transfer (PCET) may proceed *via* a stepwise mechanism in which the electron transfer is followed, in a second step, by deprotonation of the radical (ETPT, electron transfer followed by a proton transfer), or *via* a single concerted step in which both the electron and the proton are transferred in a single reaction step (CEP, concerted electron and proton transfer).[109,110]

To investigate the reaction pathway connecting the cationic to the neutral radical, we have computed a series of intermediate geometries *via* interpolation of the two corresponding optimized QM/MM structures.

The radical cation minimum structure (**VP_10ns-cat**) features a 1.079 Å N1–H1 bond length and a 1.525 Å H1–O2 (E243) bond length (see Fig. 2 and for the complete set of geometrical parameters see Table 3) while the neutral radical minimum structure (**VP_10ns-neu**) features a 1.496 Å N1–H1 bond length and a 1.076 Å H1–O2 (E243) bond length.

A transition state (TS) search has been started at the energy maximum leading to a structure (**VP_10ns-TS**) having a 1.227 Å N1–H1 bond length and a 1.289 Å H1–O2 (E243) bond length.

The QM/MM energy profile for the proton-transfer pathway is shown in Fig. 2 along with the relevant geometrical parameters that characterize the reaction coordinate. The B3LYP/6-31G**#:CHARMM calculations predict a stepwise proton transfer with a barrier of 2.3 kcal mol^{-1} and an exothermicity of 3.1 kcal mol^{-1}§.

The computed barrier is compatible with a rather facile proton transfer process that follows the electron transfer and favors the formation of a more stable neutral radical. Moreover, the TS geometry is much closer in structure and energy to the reactant, *i.e.*, the radical cation structure, than to the product, *i.e.*, the neutral radical structure, in agreement with the Hammond postulate that predicts, for exothermic reactions, a TS resembling the reactant.

Such energy profiles are consistent with the experimental finding that the tryptophan radical cation cannot be detected in VP by EPR, even using freeze quench EPR experiments with a time resolution of ms. In fact, simple considerations based on the Arrhenius law, suggests that the magnitude of

§ Single-point calculations at the QM/MM (B3LYP/6-31G**#:CHARMM) optimized structures were also carried out using (i) a larger basis set (*i.e.*, the cc-pVTZ basis set implemented in MOLCAS) and (ii) the *ab initio* multireference-perturbation-theory method (CASPT2)[115] (see the ESI†).

Table 2 B3LYP/TZVP *g*-tensors, hfcc (mT) and Mulliken spin densities computed at the QM/MM optimized geometries of neutral tryptophan radical **VP_Xns-neu** (X = 9.2, 9.4, 9.6, 9.8)

		VP_Xns-neu			
		X = 9.2	X = 9.4	X = 9.6	X = 9.8
g-tensors					
g_i	iso	2.00286	2.00286	2.00287	2.00286
	x	2.00352	2.00351	2.00354	2.00352
	y	2.00274	2.00275	2.00274	2.00275
	z	2.00233	2.00232	2.00232	2.00232
hfcc					
A_i(H-β1)	iso	2.66	2.61	2.61	2.60
	x	2.53	2.48	2.48	2.47
	y	2.85	2.80	2.80	2.78
	z	2.60	2.55	2.55	2.53
A_i(H-β2)	iso	0.94	0.97	0.91	0.96
	x	0.88	0.91	0.85	0.89
	y	0.83	0.86	0.80	0.85
	z	1.11	1.15	1.08	1.13
A_i(H1)	iso	−0.06	−0.05	−0.08	−0.05
	x	−0.21	−0.19	−0.23	−0.19
	y	0.19	0.19	0.18	0.20
	z	−0.16	−0.15	−0.18	−0.15
A_i(H2)	iso	−0.21	−0.18	−0.23	−0.20
	x	−0.36	−0.32	−0.34	−0.35
	y	0.06	0.08	0.05	0.06
	z	−0.33	−0.29	−0.39	−0.32
A_i(H-5)	iso	−0.51	−0.51	−0.51	−0.51
	x	−0.74	−0.75	−0.75	−0.74
	y	−0.22	−0.22	−0.22	−0.22
	z	−0.56	−0.57	−0.56	−0.56
A_i(H-7)	iso	−0.43	−0.42	−0.41	−0.42
	x	−0.14	−0.14	−0.13	−0.14
	y	−0.68	−0.66	−0.66	−0.68
	z	−0.46	−0.45	−0.44	−0.46
A_i(N1)	iso	0.23	0.25	0.23	0.24
	x	−0.08	−0.08	−0.07	−0.08
	y	−0.09	−0.09	−0.09	−0.09
	z	0.86	0.91	0.86	0.88
Spin densities[a]					
N1		0.19	0.20	0.19	0.19
C2		0.01	0.01	0.02	0.01
C3		0.56	0.57	0.55	0.56
C4		−0.19	−0.20	−0.19	−0.19
C5		0.25	0.26	0.25	0.25
C6		−0.09	−0.09	−0.09	−0.09
C7		0.19	0.19	0.18	0.19
C8		0.02	0.02	0.02	0.02
C9		0.06	0.06	0.06	0.06
Cβ		−0.03	−0.03	−0.03	−0.03

[a] Calculated Mulliken spin densities for nitrogen and carbons of the indolic ring and for Cβ. The total Mulliken spin density is equal to one adding the small contributions from the remaining QM atoms.

Table 3 Selected geometrical parameters[a] for QM/MM optimized structures of neutral tryptophan radical, tryptophan radical cation and resting state (RS) in VP. For abbreviations see text

System	ϕ	N1–H1	N1–C2	N1–C9	C2–C3	C3–C4	C4–C5	C4–C9	C5–C6	C6–C7	C7–C8	C8–C9	H1–O2	θ_1[c]	θ_2[c]	ρ_{C3}[c]
2BOQ[b]	−21.074	0.993	1.383	1.367	1.365	1.429	1.391	1.414	1.415	1.415	1.374	1.413	1.860			
VP_10ns-RS	−23.416	1.024	1.382	1.380	1.377	1.447	1.407	1.422	1.391	1.410	1.391	1.401	1.864			
VP_10ns-cat	−22.033	1.079	1.323	1.408	1.446	1.426	1.410	1.420	1.398	1.397	1.417	1.379	1.525	−7.8	−52.2	0.47
VP_10ns-TS	−21.792	1.227	1.322	1.411	1.452	1.422	1.409	1.419	1.399	1.399	1.414	1.378	1.289	−7.4	−52.6	0.50
VP_10ns-neu	−21.882	1.496	1.318	1.419	1.452	1.427	1.406	1.421	1.400	1.396	1.416	1.383	1.076	−8.3	−51.7	0.53
Fix-VP_10ns-cat	−22.567	1.060	1.326	1.407	1.445	1.424	1.411	1.420	1.399	1.398	1.417	1.378	1.636	−6.9	−53.1	0.46
fix-VP_10ns-neu	−22.236	1.507	1.321	1.418	1.451	1.427	1.404	1.421	1.401	1.398	1.414	1.381	1.067	−7.0	−53.0	0.53

[a] Distances in Å; angles in degrees. [b] X-Ray structure (2BOQ) with hydrogen atoms added and minimized using NAMD2.6 and CHARMM27 force field. [c] Dihedral angles θ_1 and θ_2 and spin density ρ_{C3} are obtained by solving the McConnell relationships, using the program developed by Svistunenko (freely available at the URL http://privatewww.essex.ac.uk/~svist/) and providing the computed A_{iso}(H-β1) and A_{iso}(H-β2) values ($B'' = 5.0$ mT). Results obtained solving the equations by using experimental isotropic hfcc for H-β1 (2.60 mT) and H-β2 (1.15 mT) are: $\theta_1 = -10.8 \pm 5°$; $\theta_2 = -49.2 \pm 5°$; $\rho_{C3} = 0.54$.

computed barriers are compatible with a cationic radical lifetime of few ps. The cationic radical could have been detected only in the presence of a computed barrier of at least 14 kcal mol^{-1}. Nevertheless, the presence of a barrier suggests that the proposed stepwise mechanism is still compatible with the formation of a short-lived transient radical cation.

In addition, at physiological pH, the presence of a stable tryptophan radical cation must involve some kind of stabilization by the environment. In fact, indole radicals are formed at highly oxidizing potentials and exist, in solution, as equilibrium of neutral and cationic forms having a pK_a of ~4. An example where a tryptophan radical cation has been detected is the Cyt c Peroxidase.[111] In this enzyme, the cation is stabilized by a negatively charged aspartate very close to the tryptophan radical.

In VP, due to its higher activity at acidic pH, all experimental measurements were carried out at pH = 4.5 where the neutral and cationic forms of the radical could be in equilibrium. To identify which are the contributions of the environment that favour the neutral form, as predicted by the experimental and computational results, the electrostatic potential generated by the protein residues and solvent molecules on the radical species was analyzed. In the presence of the tryptophan radical cation, the electrostatic potential is computed to be only slightly negative due to the counterbalancing effect of two positively charged residues (R257 and K253) and the nearby negatively charged E243 (see circles in Fig. 3). On the other hand, the highly positive electrostatic potential generated by the protein, following the proton transfer, strongly stabilizes the simultaneous increase of the negative charge on the nitrogen (going from –0.14 to –0.37, see bars in Fig. 3) thus shifting the equilibrium towards the neutral form. Hence, we believe that the electrostatic effects of the environment are compatible with the formation of a short-lived cationic species that evolves, in a stepwise mechanism, to the more stable neutral tryptophan radical.

EPR parameters computed on the intermediate geometries, obtained *via* interpolation, revealed an interesting trend in the Mulliken spin densities and isotropic hfcc values. Fig. 4(A) and (B) shows how these two magnetic properties, for selected atoms, change along the reaction coordinate going from the tryptophan cation to the neutral radical. It is evident that following the increase of N1–H1 bond length and corresponding decrease of H1–O2 bond length, there is a regular increasing of Mulliken spin density on C3 and N1, although larger on C3, while the spin density on C2 regularly decreases.

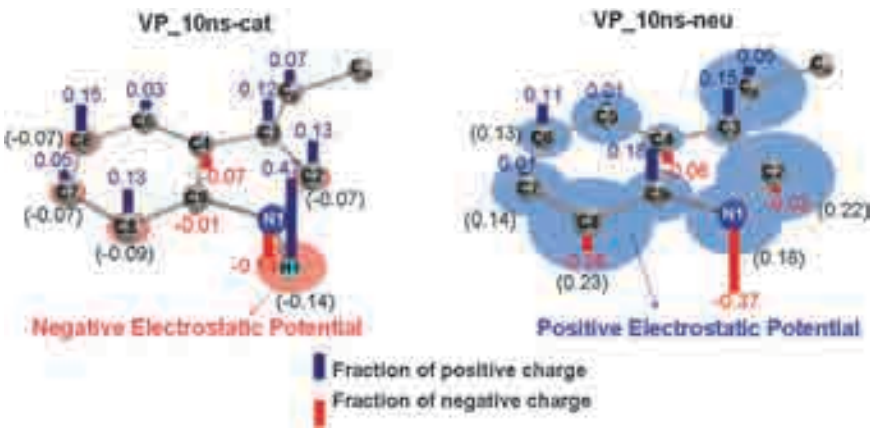

Fig. 3 Change in the charge distribution along the indole moiety between tryptophan radical cation (**VP_10ns-cat**, left side) and neutral tryptophan radical (**VP_10ns-neu**, right side). Fraction of positive (blue) or negative (red) charge is shown with coloured bars along with the corresponding values. The electrostatic potential exerted by the whole system on the indole atoms is depicted as red circles (negative) or blue circles (positive); values of the electrostatic potential that affects selected atoms are given in brackets.

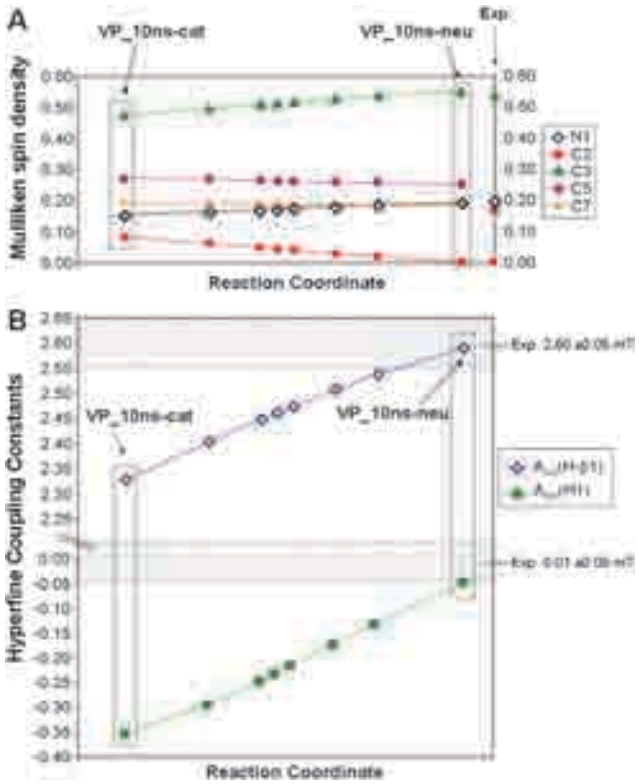

Fig. 4 Change in (A) Mulliken spin densities on selected atoms and (B) isotropic hfcc of H-β1 and H1 along the proton transfer reaction coordinate in **VP-10ns**. Gray areas indicate the range of experimental values (considering the experimental error for hfcc of ±0.05 mT).

Mulliken spin densities on C5 and C7 remain almost constant. A similar behaviour has been found for isotropic hfcc values for H-β1 that increase consistently with the increase in spin density on C3 going from the cationic to the neutral radical form. At the same time, the isotropic hfcc values for H1 become smaller along the reaction coordinate.

These trends are in accordance to the common accepted main differences characterizing the EPR magnetic properties of neutral and cationic radical species.[108] We see that Mulliken spin densities and hfcc approach the experimental values only when the more stable tryptophan neutral radical is formed¶.

Geometrical details

B3LYP/6-31G**#:CHARMM geometries of **VP_10ns-neu**, **VP_10ns-cat**, **VP_10ns-TS** are shown in Table 3 and are compared to the geometries of the optimized **VP_10ns-RS** and the X-ray structure (**2BOQ**).

¶ Further calculations made on a QM/MM optimized geometry of a neutral tryptophan radical not hydrogen bonded, obtained after breaking the N1–H1 hydrogen bond with E243 and allowing E243 to form a hydrogen bond with a nearby water molecule, gave hfcc and Mulliken spin density values beyond that of the neutral species and noticeably in disagreement with the experimental ones (see the ESI†). Indeed, computed EPR properties on this structure, exhibit deviations in isotropic hfcc for H-β1 (2.85 mT) of 0.2 mT and larger Mulliken spin density on N1 (0.25) and C3 (0.61). In addition, the computed g_x value (2.00376) is shifted of 240 ppm and is further from the experimental data (considering that the experimental error is of only ±100 ppm).

With the exception of the N1–H1 and H1–O2 bond distances the overall geometrical parameters do not significantly change between these structures. Even the spatial orientation of the tryptophan side chain, ϕ, varies within only ~2 degrees.

The dihedral angles (θ_1, θ_2) between the p_z axis (*i.e.* the p_z orbital of C3) and the projected Cβ–Hβ1,2 bonds (see Scheme 3) can be derived, together with the spin density on C3, using the semi-empirical McConnell relationships (providing computed or experimental A_{iso}(H-β1) and A_{iso}(H-β2)):

$$A_{iso}(\text{H-}\beta1) = \rho_{C3}(B' + B''\cos^2\theta_1)$$

$$A_{iso}(\text{H-}\beta2) = \rho_{C3}(B' + B''\cos^2\theta_2)$$

where B' and B'' are empirical constants ($B' = 0$, $B'' = 5$ mT).[12,19,112] As shown in Table 3, the values for θ_1, θ_2 obtained using computed isotropic hfcc values are in good agreement with those obtained using the experimental hfcc values ($\theta_1 = -10.8 \pm 5°$; $\theta_2 = -49.2 \pm 5°$). The optimized value of the angle between the two β-methylene protons is ~117°. Similar to what has been shown for tyrosyl radicals by Svistunenko *et al.*,[100] the computed value is less than the value of 120° traditionally assumed on the basis of symmetry. This could affect the difference in between the experimentally derived ρ_{C3} and Mulliken spin density and should therefore be taken into account.

The values of θ_1 and θ_2 for the cationic and neutral species are very similar and thus cannot be used to distinguish between the two forms. *Vice versa*, differences in $\rho_{C3}B''$ values, calculated using the semi-empirical McConnell relationships for neutral and cationic models of tryptophan radicals in VP are more pronounced. In fact, $\rho_{C3}B''$ varies from ~2.3 mT, for the radical cation, to ~2.7 mT for the neutral species. This latter value is in good agreement with the one (~2.7 mT) derived using the experimental A_{iso}(H-β1) and A_{iso}(H-β2) values. Furthermore, $\rho_{C3}B''$ values computed for the radical cation are below the lower limit of the $\rho_{C3}B''$ range of values reported in literature for tryptophan radicals (2.40 to 2.95 mT), which were, in most cases, identified as neutral radicals.

The comparable values of ϕ dihedral angles for the computed QM/MM systems (**VP_10ns-neu**, **VP_10ns-cat**, **VP_10ns-TS**, **VP_10ns-RS**) and the X-ray structure (**2BOQ**), show that the oxidation of the tryptophan residue does not significantly affect its spatial orientation. Furthermore, two systems featuring the same protein backbone and side-chain conformations of the X-ray structure (**2BOQ**), **fix-VP_10ns-cat** and **fix-VP_10ns-neu**, provide very similar computed EPR parameters (see Table 1, fourth and fifth columns), making clear that for VP, the X-ray structure is a good starting model for our computational studies.

The geometry of side chains of residues near W164 in **VP_10ns** and in **2BOQ** is very similar. The only difference is due to R257 side chain which, during the 10 ns MD simulation, is dynamically stabilized in a different conformation from that found in the X-ray structure. In fact, as reported in Fig. 5, R257 side chain orientation in **VP_10ns-neu** (shown in blue)

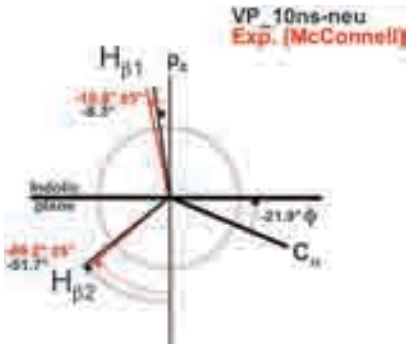

Scheme 3 θ_1 and θ_2 are defined as the dihedral angles between the p_z axis (*i.e.*, the p_z orbital of C3) and the projected Cβ–Hβ1 and Cβ–Hβ1 bonds. The comparison between θ_1 and θ_2 dihedral angles derived using McConnell relationships for computed (**VP_10ns-neu**) and experimental A_{iso}(H-β1) and A_{iso}(H-β2) is shown.

differs from the one in **fix-VP_10ns-neu** (shown in red), that corresponds to the most populated conformation of R257 in **2BOQ**. It also differs from the less populated conformation of R257 in **2BOQ** (shown in green). As mentioned above, this conformational change of R257 does not cause significant variations in the computed EPR magnetic properties.

Environmental effects

One of the goals of the present paper is to clarify the role of the protein environment in determining the magnetic properties of W164 radical. In view of that, the g_x and A_{iso}(H-β1) values are computed for the isolated neutral tryptophan radical (see **1** in Fig. 6) taken with its protein-optimized geometry (**VP_10ns-neu**) and for several different systems where the electrostatic effect of few selected amino acids near tryptophan (within ~5 Å) are added to **1**. These values are then compared with that of the whole VP system (**VP_10ns-neu**), which represents the best agreement with the experimental values, in order to determine the effect of specific residues and water molecules. As shown in Fig. 6, the g_x value of **1** is very distant from the value for **VP_10ns-neu** even if they have the same optimized geometry. On the other hand, its A_{iso}(H-β1) value, that is much more dependent on the geometry, comes closest to the value of **VP_10ns-neu**. The g_x values are significantly improved (and to a lesser extent the values of the A_{iso}(H-β1)) by adding to **1** the electrostatic effect of E243 (**2**) that confirms its critical role. However, a better agreement is reached in the presence of K253 (**4**), a positively charged residue. Surprisingly, another positively charged residue, R257 (**3**), leads to a completely opposite effect moving g_x and A_{iso}(H-β1) values away from that of **VP_10ns-neu** and it worsens in a system where both R257 and K253 are present (**6**). These contrasting effects come along with specific changes of the electrostatic potential acting on the radical centres. In fact, the computed electrostatic potential that correctly reproduces the real environment, returning g_x and A_{iso}(H-β1) values of **VP_10ns-neu**, is closely represented by **4** (1.76 *vs.* 1.57 for **VP_10ns-neu**). Considering that other residues close to tryptophan could have a relevant effect, the role of V160 (**7**), E161 (**8**) and M247 (**9**) residues was inspected. V160 does not improve the g_x and A_{iso}(H-β1) values compared to **6** while E161 and M247 give a more consistent shift in g_x value towards **VP_10ns-neu**. Furthermore, the addition of water molecules within a distance of 5 Å around any tryptophan atoms (**10**) provides a g_x value very close to **VP_10ns-neu** while the A_{iso}(H-β1) is not considerably improved.

These results suggest that an inclusion of all the protein residues and water molecules is necessary to obtain accurate values while the incomplete addition of residues could have contrasting effects that partially cancel each other. Our analysis also reveals that E243 and K253 residues are mainly responsible for the EPR spectrum of tryptophan radical in VP.

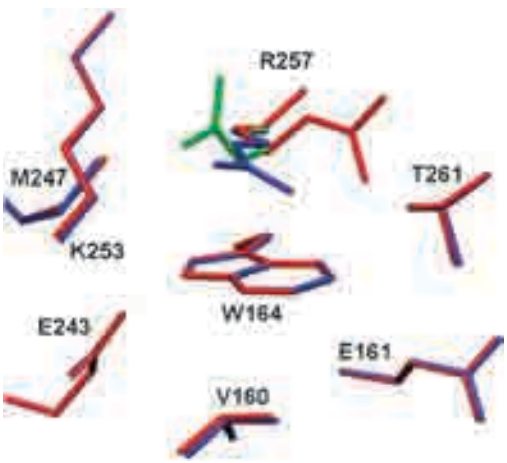

Fig. 5 Overlap between the QM/MM optimized geometries of **VP_10ns-neu** (blue) and **fix-VP_10ns-neu** (red). The major difference between the two structures is due to the different side chain orientation of R257. The other conformation of R257, less populated, found in 2BOQ crystal structure is shown in green.

2. W164Y

Tyrosyl radicals show a significantly larger *g*-tensor anisotropy than tryptophan radicals due to the large spin density on oxygen. In fact, nuclei such as oxygen or sulfur, contrary to carbon or nitrogen, have a considerable spin orbit coupling constant which gives rise to a bigger Δg_x ($\Delta g_x = g_x - g_{electron}$). For tyrosyl radicals, typical *g*-tensor values are: g_x = 2.0092–2.0068, g_y ~2.0044, and g_z ~2.0022.

The presence of a large range of g_x values depends on the different type of environments embedding the tyrosyl radicals.

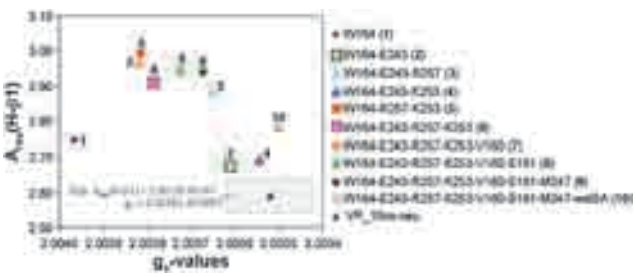

Fig. 6 Computed isotropic hfcc of H-β_1 are plotted against g_x values for the neutral tryptophan radical, taken with its protein-optimized geometry in **VP_10ns-neu**, and adding the electrostatic effect of selected amino acids in the active site region surrounding W164. The gray area indicates the range of experimental values (considering the experimental error for g_x of ±0.0001 and for hfcc of ±0.05 mT).

Higher g_x values are associated with a hydrophobic environment while a strong electronegative surroundings or the existence of hydrogen bonds significantly decrease the value of g_x.[6,105]

Considering the high sensitivity of g_x values, the EPR parameters calculations on W164Y were performed for **W164Y_10ns-A** that features the phenolic H1 proton completely transferred to the O2 carboxylic oxygen of E243 (see Fig. 7a) and for **W164Y_10ns-B** in which the H1 (transferred to E243) forms a hydrogen bond with the oxygen of a nearby water molecule (wat-A, see Fig. 7b).

B3LYP/TZVP parameters of **W164Y_10ns-A** and **W164Y_10ns-B** are shown in Table 4 (second and third columns) and are compared with experimental values from ref. 38 (first column)§.

It is evident from this comparison that the agreement between computed g_x tensor values and the experimental ones is reached only for **W164Y_10ns-B** (see Scheme 4 for the *g*-tensor orientation). In fact, for **W164Y_10ns-A**, the computed g_x value is shifted, compared to the experimental g_x value, of about 2×10^3 ppm, which is one order of magnitude larger than the experimental error (±200 ppm). Instead, the g_x value computed for **W164Y_10ns-B** is within the acceptable range of experimental values. However, the expected *g*-tensor anisotropy is well reproduced by the B3LYP/TZVP parameters of both structures reported in Table 4.

It is worthwhile to note that, in absence of the high-field EPR spectrum (W-band) for W164Y, the computed *g*-tensor values are compared with those from a CW X-band EPR spectrum. As previously reported,[45] even though X-band spectra are not very sensitive to the *g*-factor variation, the simulated spectra show an appreciable shift in isotropic g value (g_{iso}) for values of g_x lower or higher than 2.0087 (±0.0002). The sensitivity of g_{iso} has been analyzed considering that g_y and g_z are quite constant with values of g_y = 2.0041, and g_z = 2.0019.

However, the QM/MM method employed in this work turns out to be very accurate in the prediction of the EPR spectrum of the tryptophan radical in VP. This can be considered a good calibration test of the computational method since the computed data have been compared with the available experimental data obtained using multifrequency EPR and ENDOR techniques. Hence, despite the uncertainty on experimental g_x values and taking into account the acceptable range of g_x values (2.0085–2.0089), it is possible to claim that the calculated values for **W164Y_10ns-B** are a good fit for the X-band EPR spectrum of Y164 in W164Y.

As shown in Fig. 7b, **W164Y_10ns-B** features a tyrosyl radical H-bonded (2.012 Å) to the side chain of R257 residue which is in accord with previous calculations on a simple model (Tyr + H_2O) where the influence of a possible hydrogen bond on the EPR spectrum of tyrosyl radical has been simulated using as hydrogen donor a water molecule.[45] Indeed, it has been shown that the calculated *g*-tensors and hfcc values are in good agreement with the experimental ones for the case in which the water molecule is at a distance around

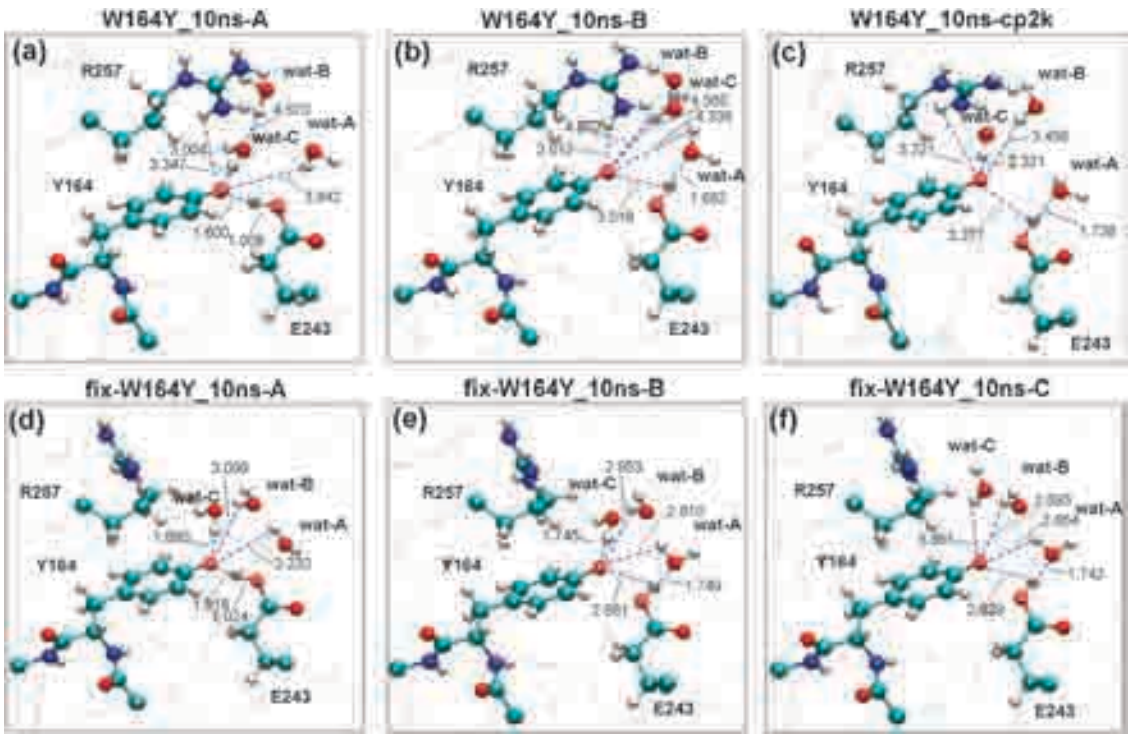

Fig. 7 QM/MM optimized geometries of tyrosyl radical in W164Y: (a) structure obtained directly from the QM/MM optimization of **W164Y_10ns** (R257 flipped); (b) structure obtained from **W164Y_10ns** where E243 is allowed to form a hydrogen bond with a nearby water molecule; (c) last snapshot from 1 ps of QM/MM MD simulation run; (d) structure obtained directly from the QM/MM optimization of **fix-W164Y_10ns** (R257 not flipped); (e) structure built from **fix-W164Y_10ns** to reproduce a hydrogen bond network similar to that of **W164Y_10ns-cp2k**; (f) structure built to show the effect of a slightly different hydrogen bond network of (e). The main hydrogen bond distances in the tyrosyl radical active site are reported in Å.

Table 4 B3LYP/TZVP *g*-tensors, hfcc (mT) and Mulliken spin densities computed at different QM/MM optimized geometries of W164Y tyrosyl radical in comparison with EPR experimental data[a] and results from previous *in vacuo* and PCM[b] calculations

			B3LYP/TZVP//B3LYP/6-31G**#		B3LYP/TZVP//BLYP/TZV2P			
		VP Exp.[a]	W164Y_10ns-A	W164Y_10ns-B	W164Y_10ns-cp2k	Tyr + H_2O	*in vacuo*[b] Tyr + H_2O	PCM[b]
g-tensors								
g_i	iso	2.0049	2.0045	2.0053	2.0052	2.0055	2.0050	
	x	2.0087	2.0067	2.0089	2.0086	2.0095	2.0081	
	y	2.0041	2.0046	2.0047	2.0047	2.0049	2.0047	
	z	2.0019	2.0023	2.0023	2.0023	2.0022	2.0022	
hfcc								
A_i(H-β1)	iso	2.15	2.54	2.33	2.27	2.21	2.40	
	x	2.20	2.70	2.47	2.42	2.34	2.54	
	y	2.09	2.42	2.21	2.17	2.11	2.30	
	z	2.16	2.51	2.29	2.21	2.17	2.37	
A_i(H-β2)	iso	0.71	0.59	0.61	0.67	0.66	0.72	
	x	0.64	0.53	0.54	0.61	0.60	0.67	
	y	0.87	0.74	0.75	0.81	0.79	0.86	
	z	0.62	0.51	0.53	0.59	0.58	0.64	
A_i(H2)	iso	0.18[c]	0.16	0.21	0.20	0.24	0.20	
	x	0.18[c]	0.14	0.19	0.19	0.22	0.19	
	y	0.27[c]	0.28	0.33	0.32	0.37	0.32	
	z	0.08[c]	0.05	0.10	0.09	0.14	0.10	
A_i(H6)	iso	0.18[c]	0.17	0.21	0.25	0.22	0.19	
	x	0.18[c]	0.16	0.20	0.22	0.20	0.18	
	y	0.27[c]	0.29	0.33	0.40	0.35	0.31	
	z	0.08[c]	0.06	0.10	0.14	0.12	0.09	
A_i(H3)	iso	0.70[c]	−0.51	−0.60	−0.61	−0.70	−0.66	
	x	1.00[c]	−0.78	−0.90	−0.93	−1.03	−0.97	
	y	0.36[c]	−0.16	−0.22	−0.23	−0.28	−0.25	
	z	0.75[c]	−0.59	−0.68	−0.67	−0.79	−0.75	
A_i(H5)	iso	0.70[c]	−0.59	−0.62	−0.65	−0.64	−0.61	
	x	1.00[c]	−0.89	−0.93	−0.96	−0.95	−0.90	
	y	0.36[c]	−0.20	−0.23	−0.26	−0.73	−0.22	
	z	0.75[c]	−0.67	−0.70	−0.74	−0.25	−0.70	
Spin densities[d]								
C1		0.38[e]	0.42	0.42	0.43	0.37	0.37	
C2		−0.08[e]	−0.12	−0.14	−0.16	−0.12	−0.11	
C3		0.25[e]	0.23	0.28	0.29	0.26	0.24	
C4		−0.05[e]	0.03	−0.03	−0.06	−0.04	0.01	
C5		0.25[e]	0.26	0.28	0.28	0.28	0.26	
C6		−0.08[e]	−0.13	−0.15	−0.15	−0.13	−0.11	
O1		0.29[e]	0.31	0.35	0.36	0.38	0.35	
Cβ		—	−0.04	−0.04	−0.04	−0.02	−0.03	

[a] Experimental data from ref. 38. The *g*-tensor values are given with a maximum error of ±0.0002. Hfcc (mT) are given with an estimated error of ±0.05 mT. [b] Calculated values from ref. 45, both *in vacuo* and adding the bulk solvent effects *via* PCM, for a neutral tyrosyl radical model (1-ethylphenole) deprotonated at O1, where hydrogen bond donor has been simulated using a water molecule. The structure was optimized *in vacuo* while constraining the Cα–Cβ–C1–C2 dihedral angle to the value (−28.6°) of the X-ray structure (2W23). [c] Hfcc (mT) for H2,6 and H3,5 protons are not distinguishable from EPR spectrum. [d] Calculated Mulliken spin densities for oxygen and carbons of the phenoxyl ring and for Cβ. The total Mulliken spin density is equal to one adding the small contributions from the remaining QM atoms. [e] Data from ref. 5 for Y122 tyrosyl radical in the R2 subunit of RNR.

2.25–2.50 Å. However, the computed EPR parameters for these simple models, either *in vacuo* or using PCM (see the fifth and sixth columns of Table 4), where the distance between the oxygen of tyrosine and the hydrogen of the water molecule is relaxed to its optimal value (1.925 Å), display g_x values much further from the experimental ones. Again and contrary to the tryptophan EPR spectrum, the g_x values for tyrosyl radicals show a greater sensitivity to different environments and in particular to changes in hydrogen bond distances.

Similar to tryptophan in VP, the major contribution to the spectrum lineshape of the tyrosyl radical in W164Y is given by the hfcc of the β-methylene protons, A_{iso}(H-β1) and A_{iso}(H-β2). The hfcc values for the protons on the phenolic ring (H_2, H_6 and H_3, H_5) are smaller in magnitude, more anisotropic and almost invariant (see Table 4). The computed hfcc values for **W164Y_10ns-B** are likely to produce a spectrum consistent with the experiment.

As it was done previously for VP, in order to assess the impact of different W164Y conformations on the electronic

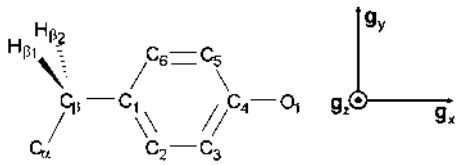

Scheme 4 Tyrosyl radical with numbering scheme and *g*-tensor principal axes orientation with respect to the molecular frame: the g_x is directed along the phenolic C4–O1 bond, g_z perpendicular to the phenyl ring plane and g_y mutually perpendicular to the other two components.

structure of tyrosyl radicals, we computed the parameters for five snapshots from the last nanosecond of MD equilibration. The five geometries were then used as starting points for QM/MM simulations after the same modifications done to construct **W164Y_10ns-B**. As shown in Table 5 for the remaining four snapshots, *g*-tensor and hfcc values change within 600 ppm and ~0.12 mT, respectively. The variation is larger than in VP especially for the g_x values, consistent with the fact that this parameter is very sensitive to the environment.[105] Nevertheless, the average (g_x = 2.00874) of the computed g_x values for the five snapshots exactly reproduces the experimental X-band g_x value.

Concerted PCET

Tyrosine oxidation results in a pK_a shift of >12 units so it is expected that the loss of the electron is accompanied by deprotonation. A mixed QM/MM based on Born–Oppenheimer molecular dynamics[86] was used to investigate the proton transfer process in W164Y. The QM/MM MD simulation demonstrates that the phenolic H1 proton of Y164 is transferred to the nearby E243 *via* a barrierless process that follows the electron transfer. Furthermore, the QM/MM MD run characterizes the full process as being an ultrafast reaction where the proton transfer occurs suddenly upon electron transfer. In fact, as shown in Fig. 8, going from 0 to 30 fs the O1–H1 distance increases from 0.986 to 1.492 Å while the H1–O2 distance decreases from 1.671 to 0.954 Å. In the following time range of 30–380 fs, the H1–O2 distance oscillates between ~1.16 and ~0.93 Å. After 380 fs, the proton transfer could be considered complete since the H1–O2 distance remains close to the distance of 1.024 Å. These results make clear that, for W164Y, the tyrosyl radical species detected by EPR is formed *via* a concerted process, where the electron and proton can be considered to be transferred in a single reaction step.

Moreover, it is evident from the QM/MM MD run that there is a reorganization of the water molecules and residues around the Y164 and E243 (see, for example, the different orientation of wat-A in Fig. 8) that assists the change in their protonation state. Meanwhile, the side chain of Y164 and E243 move away (going from 0 fs to 1 ps, the O1–O2 distance increases from ~2.65 to ~3.64 Å) allowing E243 side chain to assume its most stable conformation, forming a hydrogen bond with wat-A. The last snapshot of the 1 ps simulation (**W164Y_10ns-cp2k**) is shown in Fig. 7c, featuring the presence of a hydrogen bond (2.321 Å) between the O1 oxygen of Y164 and one hydrogen of wat-C.

The computed set of *g*-tensors, hfcc values and Mulliken spin densities for **W164Y_10ns-cp2k** (see Table 4, fourth column) is in very good agreement with the experimental values. In particular, the computed g_x value is within the experimental range of feasible g_x values (2.0085–2.0089). The EPR parameters obtained for **W164Y_10ns-cp2k** are comparable with those determined for **W164Y_10ns-B**. Accordingly, the two structures have similar features (see Fig. 7b and c): (i) the oxygen of Y164 H-bonded to R257 (2.012 Å, **W164Y_10ns-B**) or wat-C (2.321 Å, **W164Y_10ns-cp2k**). These two hydrogen bond distances permit to reproduce the experimental range of values for g_x (in agreement also with the Tyr + H_2O model system) and are longer than the hydrogen bond between Y164 and E243 (1.600 Å) found for **W164Y_10ns-A** which indeed gives a g_x value far from the experimental ones; (ii) the same side chain conformation for E243 where H1 is H-bonded to the nearby water molecule wat-A.

Geometrical details

B3LYP/6-31G**#:CHARMM geometrical parameters of **W164Y_10ns-A**, **W164Y_10ns-B**, **W164Y_10ns-cp2k** are shown in Table 6 and are compared to the geometries of the optimized resting state (**W164Y_10ns-RS**), having the tyrosine in its non-radical form, and the X-ray structure (**2W23**).

The comparison shows that, following the tyrosine oxidation, the main change concerns the reduction of the O1–C4 bond distance, varying from ~1.38 Å in the reduced Y164 (**W164Y_10ns-RS** and **2W23**) to ~1.26–1.28 Å in the radical form (**W164Y_10ns-A**, **W164Y_10ns-B**, **W164Y_10ns-cp2k**).

The spatial orientation of the tyrosine side chain defined by the ring rotation angle ϕ (Cα–Cβ–C1–C2) varies within ~6 degrees with the minimum value (~24.1°) for **W164Y_10ns-cp2k** and the maximum value (~31.2°) for **W164Y_9.2ns-B**. Consistent with the differences in the values of ϕ, the dihedral angles θ_1 and θ_2 between the p_z axis and the projected Cβ–Hβ1,2 bond (see Scheme 5) varies also within a range of ~3 degrees.

All the computed ϕ dihedral angles differ from the one measured directly from initial PDB structure (~28.6°). This variation is also larger than that found for tryptophan. Hence, the orientation of the oxidized tyrosine residue may diverge from the orientation in its reduced state. As reported by Svistunenko *et al.*,[100,113] these findings suggest that the use of these ring rotation angles to discriminate between different radical sites within the crystallographic structure, especially when these angles do not significantly differ, could lead to an erroneous assignment of the radical site given that the oxidized geometry of the radical might significantly differ from the geometry of the same residue in the resting state or X-ray structure.

The dihedral angles θ_1 and θ_2 have been derived using the same semi-empirical McConnell relationships used before for tryptophan with the only exceptions that here the considered spin density is that on C1 (ρ_{C1}) and that B'' = 5.8 mT.[114] As shown in Table 6 and similarly to what has been found for tryptophan, the values for θ_1 and θ_2 obtained using computed isotropic hfcc values are in good agreement with those obtained experimentally ($\theta_1 = -4.4 \pm 5°$; $\theta_2 = -55.6 \pm 5°$).

Table 5 B3LYP/TZVP *g*-tensors, hfcc (mT) and Mulliken spin densities computed at the QM/MM optimized geometries of W164Y tyrosyl radical: **W164Y_Xns-B** (X = 9.2, 9.4, 9.6, 9.8)

		W164Y_Xns-B			
		X = 9.2	X = 9.4	X = 9.6	X = 9.8
g-tensors					
g_i	iso	2.0051	2.0053	2.0052	2.0051
	x	2.0085	2.0091	2.0087	2.0085
	y	2.0046	2.0047	2.0046	2.0047
	z	2.0023	2.0023	2.0023	2.0023
hfcc					
A_i(H-β1)	iso	2.39	2.29	2.27	2.30
	x	2.54	2.44	2.42	2.44
	y	2.27	2.18	2.16	2.18
	z	2.36	2.26	2.24	2.26
A_i(H-β2)	iso	0.57	0.62	0.61	0.64
	x	0.51	0.55	0.55	0.57
	y	0.72	0.76	0.76	0.78
	z	0.49	0.54	0.53	0.56
A_i(H2)	iso	0.20	0.21	0.20	0.19
	x	0.18	0.18	0.19	0.18
	y	0.31	0.31	0.33	0.32
	z	0.09	0.09	0.10	0.09
A_i(H6)	iso	0.21	0.21	0.22	0.22
	x	0.20	0.20	0.20	0.20
	y	0.34	0.34	0.34	0.33
	z	0.11	0.11	0.10	0.10
A_i(H3)	iso	−0.59	−0.61	−0.59	−0.58
	x	−0.88	−0.89	−0.91	−0.90
	y	−0.21	−0.21	−0.22	−0.21
	z	−0.66	−0.67	−0.68	−0.67
A_i(H5)	iso	−0.61	−0.62	−0.63	−0.63
	x	−0.94	−0.94	−0.93	−0.91
	y	−0.23	−0.23	−0.24	−0.23
	z	−0.71	−0.71	−0.70	−0.69
Spin densities[a]					
C1		0.42	0.42	0.42	0.42
C2		−0.14	−0.14	−0.14	−0.14
C3		0.27	0.27	0.28	0.27
C4		−0.03	−0.03	−0.03	−0.02
C5		0.29	0.28	0.28	0.27
C6		−0.15	−0.15	−0.15	−0.15
O1		0.35	0.35	0.35	0.35
Cβ		−0.04	−0.04	−0.04	−0.04

[a] Calculated Mulliken spin densities for oxygen and carbons of the phenoxyl ring and for Cβ. The total Mulliken spin density is equal to one adding the small contributions from the remaining QM atoms.

The $\rho_{C1}B''$ values (~2.3 mT) calculated for **W164Y_10ns-cp2k** and **W164Y_Xns-B** tyrosyl models are very close to the one (~2.2 mT) derived using the experimental A_{iso}(H-β1) and A_{iso}(H-β2). These values are also in the range of $\rho_{C1}B''$ values (1.95 to 2.35 mT) reported in literature for tyrosyl radicals and are lower than those obtained for tryptophan radicals. Accordingly, a recent paper by Connor *et al.*[108] shows that the $\rho_C^{\pi}B''$ value (where ρ_C^{π} is the spin density on C3 for tryptophan and C1 for tyrosine) can be used to determine the identity of the two species (tryptophan or tyrosine).

In Table 6 the geometrical parameters for the five snapshots, derived from the 10 ns MD simulation and QM/MM optimized, are also reported. In contrast to the five extracted snapshots for VP (data shown in the ESI†) that do not change significantly in geometry, the five snapshots for W164Y feature differences in ϕ dihedral angle and in two distances, the one between O1 and the hydrogen of the nearby NH_2 group of R257 (see O1–H(NH) in Table 6) and the one between O1 and the hydrogen of the nearest water molecule (see O1–H(OH) in Table 6). However, a common feature of all the geometries for W164Y is the R257 orientation. During the 10 ns MD, the side chain of R257 flips (see Fig. 9) towards the phenoxyl ring of tyrosine. This conformational change is similar but more marked than that found in VP (Fig. 5). Indeed, the movement of the R257 side chain gives rise to the possibility, for the tyrosyl radical in **W164Y_Xns-B** structures, of the formation of a hydrogen bond with the NH_2 group of R257.

The flip of the R257 side chain turns to be very important in order to obtain the correct set of *g*-tensors and hfcc values. Indeed, the QM/MM optimization of three new structures (**fix-W164Y_10ns-A**, **fix-W164Y_10ns-B** and **fix-W164Y_10ns-C**, see Fig. 7d, e and f) featuring the same protein backbone and side chain conformations of the X-ray structure, *i.e.* the R257 side chain not facing the phenoxyl ring of tyrosine, gave computed EPR parameters (see Table 7) characterized by g_x values far from the experimental range (revealing shifts from the experimental g_x value of $\sim 2.7 \times 10^3$, $\sim 0.6 \times 10^3$ and $\sim 1.1 \times 10^3$ ppm, respectively). These structures were designed in order to investigate the effect of the two different R257 side chain conformations and the presence of different hydrogen bonding networks (see also next section).

Note that, in principle, structure **fix-W164Y_10ns-B**, constructed to have the same hydrogen bond network found in **W164Y_10ns-cp2k**, should give a spectrum similar to the experimental one. This is not the case, in fact, it gives a g_x value (2.0079) very different from the range of g_x ~2.0085–2.0091 found for all the structures, including **W164Y_10ns-cp2k**, that however have the R257 side chain flipped.

These results make evident that the X-ray structure of W164Y could have not been directly used as a starting model for the QM/MM optimization but a MD simulation turns out to be essential.

Hydrogen bonding and environmental effects

The results presented in this work together with previous experimental and computational findings establish that even relatively weak electrostatic perturbations can have a large effect on g_x values. Moreover, it is generally accepted that there is a clear relationship between the g_x value and the hydrogen bond strength.[6,105] The presence of hydrogen bonding, which is a special case of a more general electrostatic effect, is believed to cause a significant reduction in oxygen spin density.

The effects on the spin density distribution on O1 and C1 *versus* g_x values due to different hydrogen bond networks are displayed in Fig. 10 (the closest bond distances are shown in brackets).

It is evident that the main effect of the hydrogen bonding is to vary Mulliken spin density on O1. In fact, along with the

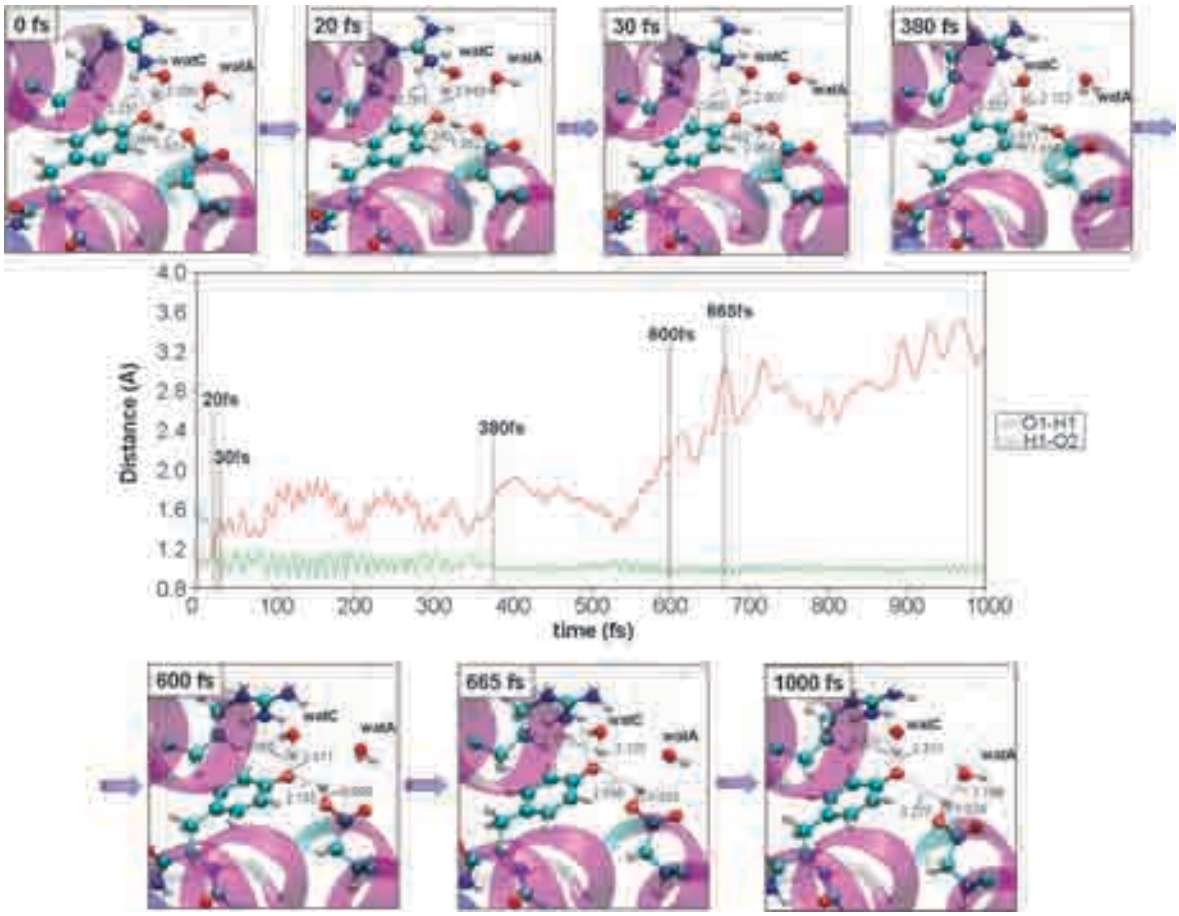

Fig. 8 Selection of snapshots resulting from the QM/MM MD simulation of tyrosyl radical in W164Y. Graph shows the variation of O1–H1 and H1–O2 bond distances (Å) during 1 ps of QM/MM MD trajectory.

Table 6 Selected geometrical parameters[a] for QM/MM optimized structures of tyrosyl radical in W164Y in comparison with resting state (RS) and crystal structure (2W23). For abbreviations see text

System	ϕ	O1–C4	O1–H1	H1–O2	C1–C2	C1–C6	C2–C3	C3–C4	C4–C5	C5–C6	O1–H(NH)[c]	O1–H(OH)[d]	θ_1[e]	θ_2[e]	ρ_{C1}[e]
2W23[b]	−28.617	1.376	0.985	1.588	1.398	1.389	1.442	1.384	1.372	1.448	4.875	1.780			
B3LYP/6-31G#**															
W164Y_10ns-RS	−29.951	1.383	0.990	1.755	1.401	1.403	1.395	1.398	1.396	1.394	2.049	2.401			
W164Y_10ns-A	−30.127	1.265	1.600	1.008	1.423	1.423	1.367	1.405	1.450	1.370	3.347	3.004	1.2	−61.2	0.45
W164Y_10ns-B	−30.225	1.257	3.018	0.990	1.420	1.420	1.373	1.451	1.455	1.369	2.012	4.335	−0.7	−59.3	0.40
W164Y_9.8ns-B	−29.128	1.258	2.911	0.997	1.421	1.420	1.371	1.457	1.454	1.369	2.022	3.312	−1.7	−58.3	0.40
W164Y_9.6ns-B	−30.013	1.258	2.690	1.000	1.420	1.418	1.372	1.453	1.449	1.369	1.928	3.233	−1.3	−58.7	0.39
W164Y_9.4ns-B	−29.946	1.257	2.996	0.995	1.420	1.421	1.373	1.456	1.452	1.370	2.017	3.290	−1.2	−58.8	0.40
W164Y_9.2ns-B	−31.251	1.257	2.882	0.994	1.420	1.421	1.375	1.457	1.447	1.367	2.056	2.755	0.7	−60.7	0.41
Fix-W164Y_10ns-A	−28.753	1.270	1.518	1.024	1.425	1.422	1.364	1.444	1.447	1.370	5.030	1.880	−1.0	−59.0	0.45
Fix-W164Y_10ns-B	−29.812	1.263	2.681	0.988	1.419	1.420	1.373	1.449	1.450	1.372	4.505	1.745	−1.3	−58.7	0.40
Fix-W164Y_10ns-C	−30.842	1.261	2.629	0.988	1.418	1.419	1.374	1.450	1.453	1.373	4.439	2.654	−0.6	−59.4	0.38
BLYP/TZV2P															
W164Y_10ns-cp2k	−24.095	1.282	3.277	1.024	1.430	1.445	1.371	1.471	1.474	1.382	3.221	2.321	−2.9	−57.1	0.39

[a] Distances in Å; angles in degrees. [b] X-Ray structure (2W23) with hydrogen atoms added and minimized using NAMD2.6 and CHARMM27 force field. [c] Distance between O1 tyrosyl oxygen and the hydrogen of the closest $-NH_2$ group of R257. [d] Hydrogen bond distance between tyrosine O1 and the nearest water molecule. [e] Dihedral angles θ_1 and θ_2 and spin density ρ_{C1} are obtained by solving the McConnell relationships, using the program developed by Svistunenko (freely available at the URL http://privatewww.essex.ac.uk/~svist/) and providing the computed A_{iso}(H-β1) and A_{iso}(H-β2) values (B'' = 5.8 mT). Results obtained solving the equations by using the experimental isotropic hfcc for H-β1 (2.15 mT) and H-β2 (0.69 mT) are: $\theta_1 = -4.4 \pm 5°$; $\theta_2 = -55.6 \pm 5°$; $\rho_{C3} = 0.37$.

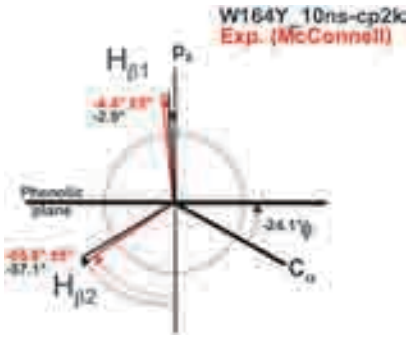

Scheme 5 θ_1 and θ_2 are defined as the dihedral angles between the p_z axis (*i.e.* the p_z orbital of C1) and the projected Cβ–Hβ1 and Cβ–Hβ2 bonds. The comparison between θ_1 and θ_2 dihedral angles derived using McConnell relationships for computed (**W164Y_10ns-cp2k**) and experimental A_{iso}(H-β1) and A_{iso}(H-β2) is shown.

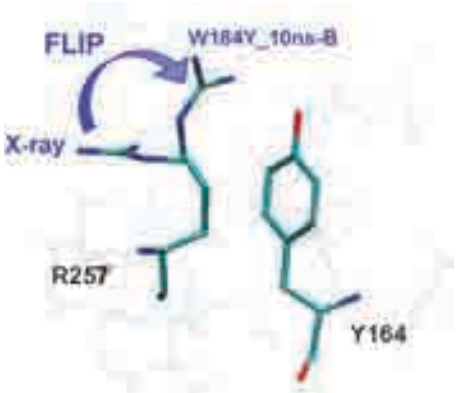

Fig. 9 Overlap between the R257 side chain conformation in the QM/MM model **W164Y_10ns-B** and the X-ray structure (2W23): the R257 dynamically flips toward the phenoxyl ring of tyrosine during the 10 ns MD run.

decrease in hydrogen bond lengths, there is a significant reduction of oxygen Mulliken spin density (the Mulliken spin density on C1 undergo smaller variations). The plot also shows that this reduction is linked to the decrease in g_x values in agreement with our previous work on Tyr + H_2O model system.[45]

The plot shown in Fig. 10 also reveals that the major shifts ($\sim 1.9 \times 10^3$ ppm) in g_x values are found going from **fix-W164Y_10ns-C** to **fix-W164Y_10ns-B**, mainly due to the formation of the hydrogen bond with wat-C, and from **fix-W164Y_10ns-B** to **fix-W164Y_10ns-A**, mainly due to the formation of the hydrogen bond with E243. The shift due to the flip of R257 (going from **W164Y_10ns-C** to **W164Y_10ns-cp2k**) is smaller ($\sim 1.2 \times 10^3$ ppm). Nevertheless, as shown previously, the R257 flip is crucial for residues and water molecules surrounding Y164 to adopt the orientation that allows the formation of the hydrogen bond network that closely reproduces the experimental results.

As shown in Fig. 11, the reduction of the oxygen spin density is, as expected, correlated to the increase in its negative charge. In fact, the polarization induced by the hydrogen bond shifts the electronic charge toward the oxygen while the spin density is shifted away from the oxygen onto the phenyl ring, especially on C2 and C6 (see Table 4 and the ESI†).

To further investigate the correlation between the sensitivity of g_x values and the electrostatic environment embedding the tyrosyl radical, g_x values are computed for the isolated Y164 radical (see **1** in Fig. 12A and B) taken with its protein-optimized geometry and for several different systems in which the electrostatic effect of few selected amino acids are added to **1**. The g_x values are reported against Mulliken spin densities on O1 and A_{iso}(H-β1) to understand the role of the environment on these magnetic properties. These values are then compared with that of the whole W164Y system (**W164Y_10ns-cp2k**), which provides the best fit with the experimental ones.

As shown in Fig. 12A, the trend between g_x values and Mulliken spin densities on O1 is confirmed. Considering the specific contribution of the selected residues around the tyrosyl radical (within ~ 5 Å), only the system including E243, R257 and K253 (**6**) gives a g_x and oxygen spin density values very close to **W164Y_10ns-cp2k**. Nevertheless, the presence of only two or one of these amino acids (system **2–5**) shifts considerably the g_x and oxygen spin density values towards **1**. This points out the relevant role of these three amino acids, taken as a whole, in determining the electrostatic environment that can reproduce the experimental g_x value.

Contrarily to VP, the cavity formed by all the residues within 5 Å (**10**) provides g_x and oxygen spin density values not in accord with experimental data. Hence, this indicates that the rest of the protein in W164Y is necessary to furnish the proper electrostatic interaction surrounding the tyrosyl radical.

As shown in Fig. 12B, it is also possible to observe a similar correlation between A_{iso}(H-β1) and g_x values. In fact, the A_{iso}(H-β1) values almost regularly increase on decreasing of the g_x values. Anyway, none of the analyzed systems reproduce the experimental value of A_{iso}(H-β1), neither system **6**, that instead provides an acceptable g_x value, nor system **10**. These results demonstrate again that the overall protein and solvent interactions are needed to obtain comparable results with the experimental data.

3. VP *vs.* W164Y

The present computational study revealed significant differences between VP and W164Y. First, in spite of the fact that a crystallographic analysis of both structures did not show marked changes after the mutation, the MD simulations and the following QM/MM optimizations of the oxidized form of the two enzymes produced, for W164Y, computed structures that differ significantly from the crystallographic one with regard to the side chain conformation of R257. Indeed, in W164Y, R257 flips from a conformation that points away from the phenoxyl ring of Y164 to a conformation where the terminal part of the side chain is facing the phenoxyl oxygen. This flip has been demonstrated to contribute to the tyrosine radical stabilization, deprotonation and transfer of H1 to E243. Moreover, it assists the reorganization of neighbouring residues and water molecules, thus allowing the formation of a proper network of hydrogen bonds. In fact, the QM/MM MD simulation has demonstrated that the approach of the positively charged group of the R257 side

Table 7 B3LYP/TZVP *g*-tensor values, hfcc (mT) and Mulliken spin densities computed at the QM/MM optimized geometries of W164Y tyrosyl radical: **fix-W164Y_10ns-A**, **fix-W164Y_10ns-B**, **fix-W164Y_10ns-C**

		B3LYP/TZVP//B3LYP/6-31G**[#]		
		fix-W164Y_10ns-A	**fix-W164Y_10ns-B**	**fix-W164Y_10ns-C**
g-tensors				
g_i	iso	2.0043	2.0049	2.0056
	x	2.0060	2.0079	2.0098
	y	2.0046	2.0046	2.0048
	z	2.0023	2.0023	2.0023
hfcc				
A_i(H-β1)	iso	2.62	2.36	2.22
	x	2.78	2.50	2.36
	y	2.49	2.24	2.11
	z	2.58	2.32	2.19
A_i(H-β2)	iso	0.69	0.64	0.58
	x	0.63	0.57	0.51
	y	0.84	0.78	0.71
	z	0.60	0.56	0.50
A_i(H2)	iso	0.12	0.19	0.21
	x	0.10	0.17	0.20
	y	0.25	0.30	0.33
	z	0.02	0.08	0.11
A_i(H3)	iso	−0.46	−0.57	−0.61
	x	−0.70	−0.86	−0.91
	y	−0.13	−0.20	−0.23
	z	−0.54	−0.65	−0.68
A_i(H5)	iso	−0.56	−0.60	−0.63
	x	−0.85	−0.90	−0.93
	y	−0.19	−0.22	−0.25
	z	−0.65	−0.68	−0.71
A_i(H6)	iso	0.15	0.19	0.22
	x	0.14	0.18	0.20
	y	0.27	0.31	0.34
	z	0.05	0.08	0.11
Spin densities[a]				
C1		0.42	0.41	0.41
C2		−0.10	−0.13	−0.15
C3		0.20	0.26	0.29
C4		0.06	−0.02	−0.06
C5		0.24	0.27	0.29
C6		−0.12	−0.14	−0.15
O1		0.29	0.35	0.38
Cβ		−0.02	−0.02	−0.02

[a] Calculated Mulliken spin densities for oxygen and carbons of the phenoxyl ring and for Cβ. The total Mulliken spin density is equal to one adding the small contributions from the remaining QM atoms.

chain allows for the breaking of the hydrogen bond with the newly protonated carboxylic group of E243 and the development of new hydrogen bonds. *Vice versa*, in VP, the R257 side chain movement is less pronounced and is not directly involved in the proton transfer from W164 to E243 since the R257 side chain moves toward the six-member ring of the indole, leaving the pyrrolic ring unperturbed.

The solvent exposed phenoxyl ring orients the large dipole moments of water molecules of the first solvation shell in such a way to provide the averaged orientation in accord with the experimental findings. This leads to a major dynamical reorganization of the solvent molecules surrounding Y164 in W164Y. On the contrary, in VP, the solvent exposed six-membered benzene ring of the tryptophan neutral radical does not significantly perturb the relative position of water molecules of the first solvation shell, leaving the environment of the neutral tryptophan radical almost unchanged.

Most importantly, the more rigid environment of VP respect to W164Y in the vicinity of the amino acid radical may also be the reason why the self-reduction of the one-electron oxidized form, VPII (see also the Introduction), is supposed to be slower in W164Y. In fact, upon oxidation, in VP, the calculations demonstrate that the H1 of the tryptophan radical is transferred to E243 but remains hydrogen bonded to N1 (with a ~1.50 Å N1–H1 bond length). This tight hydrogen bonding situation would cause a facile back transfer to N1 in the following self-reduction or reduction by a suitable substrate. In W164Y, the tyrosine oxidation is accompanied

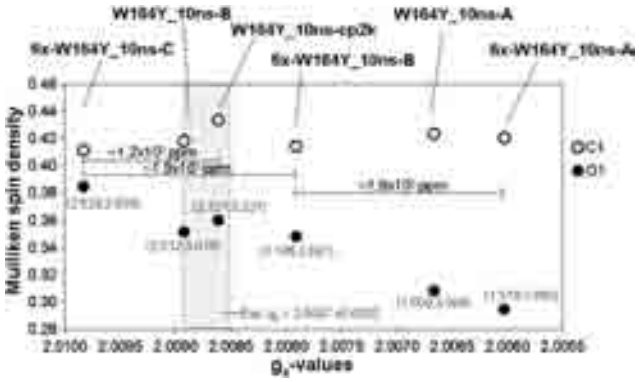

Fig. 10 Computed Mulliken spin densities on C1 and O1 plotted against g_x values for different environments of tyrosyl radical in W164Y: the closest hydrogen bond distances (Å) are shown in brackets. The differences in g_x values between different structures are given in ppm. Gray area indicates the range of experimental values (considering the experimental error for g_x of ±0.0002).

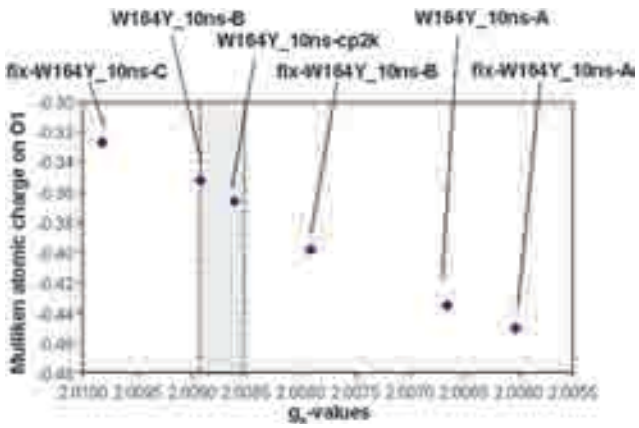

Fig. 11 Mulliken atomic charge on O1 plotted against g_x values for different environments of tyrosyl radical. Gray areas indicate the range of experimental values (considering the experimental error for g_x of ±0.0002).

by a more drastic change in the environment consisting in a conformational change of E243 and several rearrangements of the close residues and water molecules. This dynamical picture justifies a less facile re-protonation at O1, more likely by a proton delivery from the solvent, which could rationalize the slower self-reduction and substrate oxidation.

Conclusions

The following important issues have been addressed in this work.

(i) Modern DFT-based QM/MM methods are suitable for the calculations of spectroscopic properties of amino acid radicals in proteins. The calculation of EPR parameters of a tryptophan radical in VP was chosen to test the accuracy of the DFT/CHARMM approach considering that the available experimental parameters have been obtained using multi-frequency EPR and ENDOR techniques. The results clearly show that, including all the suitable electrostatic and steric environmental interactions a very good agreement with measured values can be achieved. The similarity between the computed and the experimentally derived θ_1 and θ_2 for VP and W164Y suggests that the QM/MM computed geometry correctly reproduce the oxidized form of W164 in VP and Y164 in W164Y.

(ii) The results provided by the DFT/CHARMM approach are an improvement over previous *in vacuo* or PCM calculations on Trp + H_2O and Tyr + H_2O models.

(iii) The computed set of *g*-tensors, hfcc and the Mulliken spin densities for VP, compared to the experimental data, definitively confirms the formation of a tryptophan neutral radical H-bonded at N1. The results also demonstrated that the hydrogen bond donor is the carboxylic group of E243. In particular, the calculation provided the hydrogen bond lengths and directions for the deprotonated tryptophan radical. Thus, the combination of calculated and ENDOR measured hyperfine couplings is a powerful tool for the structural characterization of hydrogen bonding geometries.

(iv) The formation of the neutral tryptophan radical is exothermic with a barrier (~2–4 kcal mol^{-1}) compatible with an ETPT process and with the existence, although it was not possible to detect experimentally, of a short-lived transient radical cation having a lifetime of few ps.

(v) A regular increase of Mulliken spin density on C3 and N1 and a concomitant decrease of the spin density on C2 has been found along the reaction coordinate going from the cation to neutral form of tryptophan radical. Consistent with the increase in spin density on C3 there is an increase of A_{iso}(H-β1) and a decrease of A_{iso}(H-1).

(vi) The QM/MM MD simulation of W164Y demonstrates that the phenolic H1 of Y164 is transferred *via* a CEP process to the nearby E243 residue that acts as the proton acceptor for both the tryptophan neutral and tyrosyl radicals (although in the former case a transient cationic species exists). In W164Y, in contrast to VP, E243 breaks the hydrogen bond with the tyrosyl radical and forms a new hydrogen bond with a nearby water molecule. Coupled to these changes there is a reorganization of water molecules and residues (especially regarding the R257 side chain conformation) around the tyrosyl radical that allows to model the protein conformation and hydrogen bonding networks that closely reproduce the experimental results. Furthermore, the different E243 side chain conformation in W164Y could be at the origin of the lowest self reduction and substrate oxidation by the variant compared to native VP, where the transferred proton remains H-bonded to tryptophan N1 and can be easily recovered by the catalytic residue in its subsequent reduction.

(vii) In W164Y, together with the decrease in hydrogen bond lengths there is a decrease of Mulliken spin density on O1 combined to an increase of g_x-values. The reduction of the oxygen spin density is, as expected, correlated to the increase in its negative charge. In addition, A_{iso}(H-β1) values increase almost regularly upon the decrease in the g_x values.

(viii) The analysis of the electrostatic potential generated by few selected amino acids and water molecules on the tryptophan and tyrosyl radicals reveals that, for VP, the residues that principally contribute to the experimental EPR parameters are E243 and K253 while, for W164Y, are E243, R257 and K253.

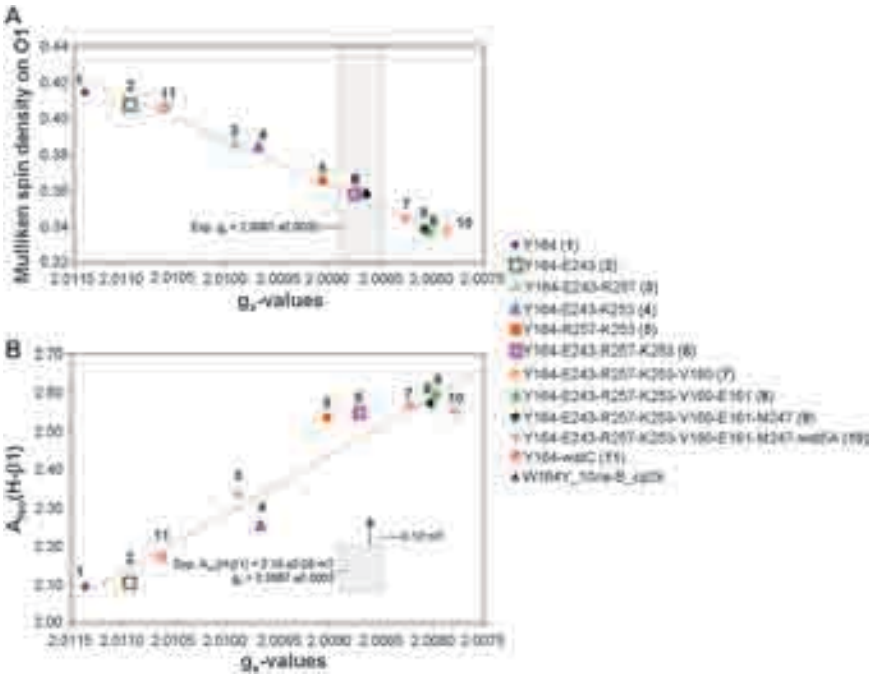

Fig. 12 Computed Mulliken spin densities on O1 (A) and isotropic hfcc of H-β_1 (B) plotted against g_x values for the tyrosyl radical taken with its protein-optimized geometry in **W164Y_10ns-cp2k**, and adding the electrostatic effect of selected amino acids in the active site region surrounding Y164. Gray areas indicate the range of experimental values (considering the experimental error for g_x of ± 0.0002 and for hfcc of ± 0.05 mT).

(ix) Following the ET process, *i.e.*, going from the reduced to oxidized form, the main structural changes in both VP and W164Y enzymes concern the pyrrolic and phenolic bond lengths, respectively. In W164Y, it is possible to observe also a greater variation of the ring rotation angle governing the spatial orientation of the Y164 radical.

Not all of these challenging issues could have been directly addressed by experimental EPR/ENDOR studies. They were therefore investigated in detail in this computational work. Provided the assessing of the inherent quality of the QM/MM procedures, it is now clear that combining spectroscopy with computational investigation, one can obtain valuable insight into the geometric and electronic structures of biologically important radical species as well an unequivocal proof of the identity of the amino acid radicals and its assignment to a specific site inside the protein. In addition, it is possible to achieve a more complete understanding at the microscopic level of what happens following the ET process that leads to the radical formation and which are the main interactions inside the protein matrix that contribute to the experimental magnetic spectroscopic parameters.

In this work, the combined use of QM/MM, QM/MM MD and DFT methods allowed for a realistic modeling of enzyme intermediates in VPs and therefore, opens new possibilities for a host of future applications. Indeed, with the aim of resolving the mechanism controlling the degradation of substrates, new studies will be performed. These studies could well provide insight into the difference in catalytic activity of W164Y as compared to VP and may very well make possible *de novo* design of new variants or enzymes with higher activity or different desirable properties.

Acknowledgements

This work was supported by the Italian MIUR PRIN 2007 project and the BIORENEW EU-project fundings.

We thank CINECA for granted calculation time.

F. J. R.-D. thanks the Spanish MICINN for a Ramon y Cajal contract.

Careful reading and revising of the manuscript by Professor Emeritus Les Brooks (Sonoma State University) is gratefully acknowledged.

Notes and references

1 J. Stubbe and W. A. Der Donk, *Chem. Rev.*, 1998, **98**, 705.
2 C. Aubert, M. H. Vos, P. Mathis, A. P. M. Eker and K. Brettel, *Nature*, 2000, **405**, 586.
3 J. Stubbe, D. G. Nocera, C. S. Yee and M. C. Y. Chang, *Chem. Rev.*, 2003, **103**, 2167.
4 P. Reichard and A. Ehrenberg, *Science*, 1983, **221**, 514.
5 C. W. Hoganson, M. Sahlin, B.-M. Sjöberg and G. T. Babcock, *J. Am. Chem. Soc.*, 1996, **118**, 4672.
6 S. Un, C. Gerez, E. Elleingand and M. Fontecave, *J. Am. Chem. Soc.*, 2001, **123**, 3048.
7 M. Galander, M. Uppsten, U. Uhlin and F. Lendzian, *J. Biol. Chem.*, 2006, **281**, 31743.
8 P. Faller, C. Goussias, A. W. Rutherford and S. Un, *Proc. Natl. Acad. Sci. U. S. A.*, 2003, **100**, 8732.
9 C. Aubert, P. Mathis, A. P. Eker and K. Brettel, *Proc. Natl. Acad. Sci. U. S. A.*, 1999, **96**, 5423.
10 H. Pelletier and J. Kraut, *Science*, 1992, **258**, 1748.
11 T. P. Barrows, B. Bhaskar and L. P. Thomas, *Biochemistry*, 2004, **43**, 8826.
12 G. Bleifuss, M. Kolberg, S. Pötsch, W. Hofbauer, R. Bittl, W. Lubitz, A. Gräslund, G. Lassmann and F. Lendzian, *Biochemistry*, 2001, **40**, 15362.
13 J. E. Miller, C. Grădinaru, B. C. Crane, A. J. Di Bilio, W. A. Wehbi, S. Un, J. R. Winkler and H. B. Gray, *J. Am. Chem. Soc.*, 2003, **125**, 14220.

14 G. J. Gerfen, F. Licht, J.-P. Willems, B. M. Hoffman and J. Stubbe, *J. Am. Chem. Soc*., 1996, **118**, 8192.
15 C. Duboc-Toia, A. K. Hassan, E. Mulliez, S. Ollagnier-de Choudens, M. Fontecave, C. Leutwein and J. Heider, *J. Am. Chem. Soc*., 2003, **125**, 38.
16 E. Mulliez, M. Fontecave, J. Gaillard and P. Reichard, *J. Biol. Chem*., 1993, **268**, 2296.
17 P. Young, J. Andersson, M. Sahlin and B.-M. Sjöberg, *J. Biol. Chem*., 1996, **271**, 20770.
18 S. Pötsch, F. Lendzian, R. Ingemarson, A. Hornberg, L. Thelander, W. Lubitz, G. Lassmann and A. Graslund, *J. Biol. Chem*., 1999, **274**, 17696.
19 F. Lendzian, M. Sahlin, F. MacMillan, R. Bittl, R. Fiege, S. Pötsch, B.-M. Sjöberg, A. Gräslund, W. Lubitz and G. Lassmann, *J. Am. Chem. Soc*., 1996, **118**, 8111.
20 R. Pogni, M. C. Baratto, C. Teutloff, S. Giansanti, F. J. Ruiz-Duenas, T. Choinowski, K. Piontek, A. T. Martinez, F. Lendzian and R. Basosi, *J. Biol. Chem*., 2006, **28**, 9517.
21 R. Pogni, C. Teutloff, F. Lendzian and R. Basosi, *Appl. Magn. Reson*., 2007, **31**, 509.
22 M. Pérez-Boada, F. J. Ruiz-Dueñas, R. Pogni, R. Basosi, T. Choinowski, M. J. Martínez, K. Piontek and A. T. Martínez, *J. Mol. Biol*., 2005, **354**, 385.
23 F. J. Ruiz-Dueñas, M. Morales, M. Pérez-Boada, T. Choinowski, M. J. Martínez, K. Piontek and A. T. Martínez, *Biochemistry*, 2007, **46**, 66.
24 R. Pogni, M. C. Baratto, S. Giansanti, C. Teutloff, J. Verdin, B. Valderram, F. Lendzian, W. Lubitz, R. Vazquez-Duhalt and R. Basosi, *Biochemistry*, 2005, **44**, 4267.
25 H. Zorn, S. Langhoff, M. Scheibner, M. Nimtz and R. G. Berger, *Biol. Chem*., 2003, **384**, 1049.
26 T. Mester and J. A. Field, *J. Biol. Chem*., 1998, **273**, 15412.
27 M. J. Martínez, F. J. Ruiz-Duenäs, F. Guillén and A. T. Martínez, *Eur. J. Biochem*., 1996, **237**, 424.
28 F. J. Ruiz-Dueñas, M. J. Martínez and A. T. Martínez, *Mol. Microbiol*., 1999, **31**, 223.
29 A. Heinfling, M. J. Martínez, A. T. Martínez, M. Bergbauer and U. Szewzyk, *FEMS Microbiol. Lett*., 1998, **165**, 43.
30 A. Heinfling, F. J. Ruiz-Dueñas, M. J. Martínez, M. Bergbauer, U. Szewzyk and A. T. Martínez, *FEBS Lett*., 1998, **428**, 141.
31 F. J. Ruiz-Dueñas, M. Morales, M. J. Mate, A. Romero, M. J. Martínez, A. T. Smith and A. T. Martínez, *Biochemistry*, 2008, **47**, 1685.
32 Y. X. Wang, R. Vázquez-Duhalt and M. A. Pickard, *Can. J. Microbiol*., 2003, **49**, 675.
33 D. P. Barr and S. D. Aust, *Environ. Sci. Technol*., 1994, **28**, 78A.
34 H. Kamitsuji, T. Watanabe, Y. Honda and M. Kuwahara, *Biochem. J*., 2005, **386**, 387.
35 P. J. Harvey, L. P. Candeias, P. J. King, J. M. Palmer and R. Wever, *Biochem. Soc. Trans*., 1995, **23**, S340.
36 K. E. Hammel, K. A. Jensen, M. D. Mozuch, L. L. Landucci, M. Tien and E. A. Pease, *J. Biol. Chem*., 1993, **268**, 12274.
37 R. Tinoco, J. Verdín and R. Vázquez-Duhalt, *J. Mol. Catal. B: Enzym*., 2007, **46**, 1.
38 F. J. Ruiz-Dueñas, R. Pogni, M. Morales, S. Giansanti, M. J. Mate, A. Romero, M. J. Martínez, R. Basosi and A. T. Martínez, *J. Biol. Chem*., 2009, **284**, 7986.
39 T. Choinowski, W. Blodig, H. K. Winterhalter and K. Piontek, *J. Mol. Biol*., 1999, **286**, 809.
40 W. Blodig, A. T. Smith, W. A. Doyle and K. Piontek, *J. Mol. Biol*., 2001, **305**, 851.
41 W. A. Doyle, W. Blodig, N. C. Veitch, K. Piontek and A. T. Smith, *Biochemistry*, 1998, **37**, 15097.
42 W. Blodig, A. T. Smith, H. K. Winterhalter and K. Piontek, *Arch. Biochem. Biophys*., 1999, **370**, 86.
43 A. T. Smith, W. A. Doyle, P. Dorlet and A. Ivancich, *Proc. Natl. Acad. Sci. U. S. A*., 2009, **106**, 16084.
44 J. Tomasi and M. Persico, *Chem. Rev*., 1994, **94**, 2027.
45 C. Bernini, A. Sinicropi, R. Basosi and R. Pogni, *Appl. Magn. Reson*., 2010, **37**, 279.
46 A. Warshel and L. M., *J. Mol. Biol*., 1976, **103**, 227.
47 H. M. Senn and W. Thiel, *Angew. Chem., Int. Ed*., 2009, **48**, 1198.
48 M. H. M. Olsson, G. Hong and A. Warshel, *J. Am. Chem. Soc*., 2003, **125**, 5025.
49 S. Shaik, D. Kumar, S. P. de Visser, A. Altun and W. Thiel, *Chem. Rev*., 2005, **105**, 2279.
50 H. Lin and D. G. Truhlar, *Theor. Chem. Acc*., 2006, **117**, 185.
51 F. Neese, *Curr. Opin. Chem. Biol*., 2003, **7**, 125.
52 J. C. Schöneboom, F. Neese and W. Thiel, *J. Am. Chem. Soc*., 2005, **127**, 5840.
53 S. Sinnecker and F. Neese, *J. Comput. Chem*., 2006, **27**, 1463.
54 A. Altun, S. Yokoyama and K. Morokuma, *J. Phys. Chem. A*, 2009, **113**, 11685.
55 K. R. Geethalakshmi, M. P. Waller, W. Thiel and M. Bühl, *J. Phys. Chem. B*, 2009, **113**, 4456.
56 M. Sundararajan, C. Riplinger, M. Orio, F. Wennmohs and F. Neese, in *Comput. Inorg. Bioinorg. Chem*., ed. E. I. Solomon, R. A. Scott and R. Bruce King, Wiley, New York, 2009.
57 S. Pistolesi, A. Sinicropi, R. Pogni, R. Basosi, N. Ferré and M. Olivucci, *J. Phys. Chem. B*, 2009, **113**, 16082.
58 P. Cimino, A. Pedone, E. Stendardo and V. Barone, *Phys. Chem. Chem. Phys*., 2010, **12**, 3741.
59 F. Lumento, V. Zanirato, S. Fusi, E. Busi, L. Latterini, F. Elisei, A. Sinicropi, T. Andruniów, N. Ferré, R. Basosi and M. Olivucci, *Angew. Chem., Int. Ed*., 2007, **46**, 414.
60 A. Sinicropi, T. Andruniow, N. Ferrè, R. Basosi and M. Olivucci, *J. Am. Chem. Soc*., 2005, **127**, 11534.
61 A. Sinicropi, C. Bernini, R. Basosi and M. Olivucci, *Photochem. Photobiol. Sci*., 2009, **8**, 1639.
62 A. Sinicropi, E. Martin, M. Ryasantsev, J. Helbing, J. Briand, D. Sharma, J. Léonard, S. Haacke, A. Canizzo, M. Chergui, V. Zanirato, S. Fusi, F. Santoro, R. Basosi, N. Ferré and M. Olivucci, *Proc. Natl. Acad. Sci. U. S. A*., 2008, **105**, 17642.
63 F. Masson, T. Laino, U. Rothlisberger and J. Hutter, *ChemPhysChem*, 2009, **10**, 400.
64 D. Roca-Sanjuán, G. Olaso-González, P. B. Coto, M. Merchán and L. Serrano-Andrés, *Theor. Chem. Acc*., 2009, **126**, 177, DOI: 10.1007/s00214-009-0626-9.
65 R. A. Friesner and V. Guallar, *Annu. Rev. Phys. Chem*., 2005, **56**, 389.
66 V. Guallar, *J. Phys. Chem. B*, 2008, **112**, 13460.
67 R. Hart and P. J. O'Malley, *Biochim. Biophys. Acta, Bioenerg*., 2010, **1797**, 250.
68 C. S. Porro, D. Kumar and S. P. de Visser, *Phys. Chem. Chem. Phys*., 2009, **11**, 10219.
69 M. C. Colombo, J. V. VandeVondele, S. Van Doorslaer, A. Laio, L. Guidoni and U. Rothlisberger, *Proteins: Struct., Funct., Bioinf*., 2007, **70**, 1084.
70 S. Sinnecker, M. Flores and W. Lubitz, *Phys. Chem. Chem. Phys*., 2006, **8**, 5659.
71 S. Moon, S. Patchkovskii and D. R. Salahub, *THEOCHEM*, 2003, **632**, 287.
72 H. Li, A. D. Robertson and J. H. Jensen, *Proteins: Struct., Funct., Bioinf*., 2005, **61**, 704.
73 W. Humphrey, A. Dalke and K. Schulten, *J. Mol. Graphics*, 1996, **14**, 33.
74 A. D. MacKerell Jr., D. Bashford, M. Bellott, R. L. Dunbrack Jr., J. D. Evanseck, M. J. Field, S. Fischer, J. Gao, H. Guo, S. Ha, D. Joseph-McCarthy, L. Kuchnir, K. Kuczera, F. T. K. Lau, C. Mattos, S. Michnick, T. Ngo, D. T. Nguyen, B. Prodhom, W. E. Reiher III, B. Roux, M. Schlenkrich, J. C. Smith, R. Stote, J. Straub, M. Watanabe, J. Wiórkiewicz-Kuczera, D. Yin and M. Karplus, *J. Phys. Chem. B*, 1998, **102**, 3586.
75 W. L. Jorgensen, J. Chandrasekhar, J. D. Madura, R. W. Impey and M. L. Klein, *J. Chem. Phys*., 1983, **79**, 926.
76 K. Kuczera, J. Kuriyan and M. Karplus, *J. Mol. Biol*., 1990, **213**, 351.
77 J. C. Phillips, R. Braun, W. Wang, J. Gumbart, E. Tajkhorshid, E. Villa, C. Chipot, R. D. Skeel, L. Kale and S. K., *J. Comput. Chem*., 2005, **26**, 1781.
78 T. Darden, D. York and L. Pederson, *J. Chem. Phys*., 1993, **98**, 10089.
79 G. Karlström, R. Lindh, P.-A. Malmqvist, B. O. Roos, U. Ryde, V. Veryazov, P.-O. Widmark, M. Cossi, B. Schimmelpfennig, P. Neogrady and L. Seijo, *Comput. Mater. Sci*., 2003, **28**, 222.
80 J. W. Ponder 2004, Tinker4.2 - software tools for molecular design, Available at: http://dasher.wustl.edu/tinker.
81 T. Andruniow, N. Ferré and M. Olivucci, *Proc. Natl. Acad. Sci. U. S. A*., 2004, **101**, 17908.

82 N. Ferré and M. Olivucci, *THEOCHEM*, 2003, **632**, 71.
83 A. D. Becke, *J. Chem. Phys.*, 1993, **98**, 5648.
84 C. Lee, W. Yang and R. G. Parr, *Phys. Rev. B: Condens. Matter*, 1988, **37**, 785.
85 P. J. Stephens, F. J. Devlin, C. F. Chabalowski and M. J. Frisch, *J. Phys. Chem.*, 1994, **98**, 11623.
86 CP2K 2009, freely available at the URL http://cp2k.berlios.de.
87 G. Lippert, J. Hutter and M. Parrinello, *Theor. Chem. Acc.*, 1999, **103**, 124.
88 J. VandeVondele, M. Krack, F. Mohamed, M. Parrinello, T. Chassaing and J. Hutter, *Comput. Phys. Commun.*, 2005, **167**, 103.
89 T. Laino, F. Mohamed, A. Laio and M. Parrinello, *J. Chem. Theory Comput.*, 2005, **1**, 1176.
90 T. Laino, F. Mohamed, A. Laio and M. Parrinello, *J. Chem. Theory Comput.*, 2006, **2**, 1370.
91 A. Schäfer, C. Huber and R. Ahlrichs, *J. Chem. Phys.*, 1994, **100**, 5829.
92 F. Masson, T. Laino, I. Tavernelli, U. Rothlisberger and J. Hutter, *J. Am. Chem. Soc.*, 2008, **130**, 3443.
93 C. L. Stanton, I.-F. W. Kuo, C. J. Mundy, T. Laino and K. N. Houk, *J. Phys. Chem. B*, 2007, **111**, 12573.
94 S. Goedecker, M. Teter and J. Hutter, *Phys. Rev. B: Condens. Matter*, 1996, **54**, 1703.
95 C. Hartwigsen, S. Goedecker and J. Hutter, *Phys. Rev. B: Condens. Matter Mater. Phys.*, 1998, **58**, 3641.
96 W. G. Hoover, *Phys. Rev. B: Condens. Matter*, 1985, **31**, 1695.
97 S. J. Nose, *J. Chem. Phys.*, 1984, **81**, 511.
98 F. Neese, *ORCA, an* ab initio, *Density Functional and Semi-empirical Program Package*, University of Bonn, Germany, Version 2.7, June 2009.
99 V. Barone and P. Cimino, *J. Chem. Theory Comput.*, 2009, **5**, 192.
100 D. A. Svistunenko and G. A. Jones, *Phys. Chem. Chem. Phys.*, 2009, **11**, 6600.
101 B. Brogioni, D. Biglino, A. Sinicropi, E. Reijerse, P. Giardina, G. Sannia, W. Lubitz, R. Basosi and P. R., *Phys. Chem. Chem. Phys.*, 2008, **10**, 7284.
102 M. Pavone, P. Cimino, O. Crescenzi, A. Sillanpää and V. Barone, *J. Phys. Chem. B*, 2007, **111**, 8928.
103 M. van Gastel, W. Lubitz, G. Lassmann and F. Neese, *J. Am. Chem. Soc.*, 2004, **126**, 2237.
104 D. Baute, D. Arieli, F. Neese, H. Zimmermann, B. M. Weckhuysen and D. Goldfarb, *J. Am. Chem. Soc.*, 2004, **126**, 11733.
105 S. Un, *Magn. Reson. Chem.*, 2005, **43**, S229.
106 F. Neese, *JBIC, J. Biol. Inorg. Chem.*, 2006, **11**, 702.
107 F. Neese, *EPR Newslett.*, 2009, **18**, 4.
108 H. D. Connor, E. S. Bradley, M. Carolyn, J. S. Herbert, Jr. and R. P. Mason, *J. Am. Chem. Soc.*, 2008, **130**, 6381.
109 M. Sjödin, R. Ghanem, T. Polivka, J. Pan, S. Styring, L. Sun, V. Sundström and L. Hammarström, *Phys. Chem. Chem. Phys.*, 2004, **6**, 4851.
110 M. Sjödin, S. Stenbjörn, H. Wolpher, Y. Xu, L. Sun and L. Hammarström, *J. Am. Chem.Soc.*, 2005, **127**, 3855.
111 J. E. Huyett, P. E. Doan, R. Gurbiel, A. L. P. Houseman, M. Sivaraja, D. B. Goodin and B. M. Hoffman, *J. Am. Chem. Soc.*, 1995, **117**, 9033.
112 E. W. Stone and A. H. Maki, *J. Chem. Phys.*, 1962, **37**, 1326.
113 D. A. Svistunenko, M. T. Wilson and C. E. Cooper, *Biochim. Biophys. Acta, Bioenerg.*, 2004, **1655**, 372.
114 R. W. Fessenden and R. H. Schuler, *J. Chem. Phys.*, 1963, **39**, 2147.
115 K. Andersson, P.-Å. Malmqvist and B. O. Roos, *J. Chem. Phys.*, 1992, **96**, 1218.

Supplementary Material (ESI) for PCCP

EPR Parameters of Amino Acid Radicals in *P. eryngii* Versatile Peroxidase and its W164Y variant computed at the QM/MM level

Caterina Bernini,[a] *Rebecca Pogni,*[a] *Francisco J. Ruiz-Dueñas,*[b] *Angel T. Martínez,*[b]

Riccardo Basosi [a] *and Adalgisa Sinicropi* [a,*]

[a]*Department of Chemistry, University of Siena, 53100 Siena, Italy*
[b]*Centro de Investigaciones Biológicas, Consejo Superior de Investigaciones Cientificas, 28040 Madrid, Spain*

Supporting Information

Contents

1. Computational Details

1.1 Setup of the System

Initial structures for VP (pdb code: 2BOQ) and its W164Y variant (pdb code: 2W23) were obtained from the Protein Data Bank (1.33 Å and 1.94 Å resolution, respectively). The results of PROPKA2.0[1] runs were used, in combination with visual inspection, to assign the protonation states of all titratable residues (aspartic acid, glutamic acid and histidine) at the experimental pH (pH = 4.5). We assigned D30, D318, E26, E36, E40, E83, E140, E191, E217, E225 to be protonated, H39, H47, H232 to be protonated at the ε nitrogen and H169, which is coordinated to iron, to be protonated at the δ nitrogen. Missing hydrogen atoms were added by the psfgen module of VMD, version 1.8.6.[2] The protonated systems, as described above, with crystallographic water molecules, were neutralized with sodium and chlorine ions (0.15 M ionic strength) and fully solvated in a rectangular box (69 x 80 x 76 $Å^3$ for VP and 75 x 65 x 73 $Å^3$ for W164Y) of TIP3P water molecules using the autoionize and solvate modules of VMD.[2] Solvent boxes were created with a layer of at least 10 Å of water molecules around each protein atom and included 33975 and 31575 water molecules for VP and W164Y, respectively.

1.2 Force Field

All heme parameters were taken from the existing CHARMM27 library,[3] originally determined for a Fe^{2+} containing heme group,[4] with the exception that the atomic charges were modified to account for the different charge distribution in the Fe^{3+}-porphyrine complex.

Force Field atom types and charges for the heme used in the present work:

```
Atom
name
          type    charge
GROUP
ATOM FE   FE       1.68 !       O2A   O1A             O2D  O1D
ATOM NA   NPH     -0.76 !         \\ //                 \\ //
ATOM NB   NPH     -0.76 !           CGA                   CGD
ATOM NC   NPH     -0.76 !            |                     |
ATOM ND   NPH     -0.76 !    HBA1--CBA--HBA2  HA   HBD1--CBD--HBD2
ATOM C1A  CPA      0.32 !            |           |           |
ATOM C2A  CPB     -0.03 !    HAA1--CAA-HAA2  _CHA_ HAD1--CAD--HAD2
ATOM C3A  CPB     -0.02 !            |       /     \       |
ATOM C4A  CPA      0.32 !           C2A---C1A       C4D---C3D
ATOM C1B  CPA      0.32 !            |     |          |     |
ATOM C2B  CPB     -0.02 !HMA1\       |     |          |     |      /HMD1
ATOM C3B  CPB     -0.03 !HMA2-CMA--C3A    NA        ND    C2D--CMD-HMD2
ATOM C4B  CPA      0.32 !HMA3/       \   / \        / \   /       \HMD3
ATOM C1C  CPA      0.32 !             C4A   \     /   C1D
ATOM C2C  CPB     -0.03 !            /       \   /       \
ATOM C3C  CPB     -0.02 !      HB--CHB        FE         CHD--HD
ATOM C4C  CPA      0.32 !            \       /   \       /
ATOM C1D  CPA      0.32 !             C1B   /     \   C4C        HAC
```

```
ATOM C2D  CPB    -0.02 !HMB1\       /   \ /       \ /   \       /
ATOM C3D  CPB    -0.03 !HMB2-CMB--C2B    NB       NC    C3C--CAC
ATOM C4D  CPA     0.32 !HMB3/      |     |         |     |     \\  /HBC1
GROUP                 !          |     |         |     |      CBC
ATOM CHA  CPM    -0.10 !          C3B---C4B       C1C---C2C        \HBC2
ATOM HA   HA      0.10 !           |       \_CHC_/       |
GROUP                 !          CAB         |         CMC--HMC3
ATOM CHB  CPM    -0.10 !         //  \        HC       /  |
ATOM HB   HA      0.10 !        CBB  HAB           HMC1  HMC2
GROUP                 !       /   \
ATOM CHC  CPM    -0.10 !    HBB1  HBB2
ATOM HC   HA      0.10 !
GROUP
ATOM CHD  CPM    -0.10
ATOM HD   HA      0.10
GROUP
ATOM CMA  CT3    -0.27
ATOM HMA1 HA      0.09
ATOM HMA2 HA      0.09
ATOM HMA3 HA      0.09
GROUP
ATOM CAA  CT2    -0.18
ATOM HAA1 HA      0.09
ATOM HAA2 HA      0.09
GROUP
ATOM CBA  CT2    -0.28
ATOM HBA1 HA      0.09
ATOM HBA2 HA      0.09
ATOM CGA  CC      0.62
ATOM O1A  OC     -0.76
ATOM O2A  OC     -0.76
GROUP
ATOM CMB  CT3    -0.27
ATOM HMB1 HA      0.09
ATOM HMB2 HA      0.09
ATOM HMB3 HA      0.09
GROUP
ATOM CAB  C      -0.20
ATOM HAB  HA      0.20
GROUP
ATOM CBB  C      -0.20
ATOM HBB1 HA      0.10
ATOM HBB2 HA      0.10
GROUP
ATOM CMC  CT3    -0.27
ATOM HMC1 HA      0.09
ATOM HMC2 HA      0.09
ATOM HMC3 HA      0.09
GROUP
ATOM CAC  C      -0.20
ATOM HAC  HA      0.20
GROUP
ATOM CBC  C      -0.20
ATOM HBC1 HA      0.10
ATOM HBC2 HA      0.10
GROUP
ATOM CMD  CT3    -0.27
ATOM HMD1 HA      0.09
ATOM HMD2 HA      0.09
ATOM HMD3 HA      0.09
GROUP
ATOM CAD  CT2    -0.18
ATOM HAD1 HA      0.09
```

```
ATOM HAD2 HA      0.09
GROUP
ATOM CBD  CT2    -0.28
ATOM HBD1 HA      0.09
ATOM HBD2 HA      0.09
ATOM CGD  CC      0.62
ATOM O1D  OC     -0.76
ATOM O2D  OC     -0.76
```

1.3 QM/MM Method

All QM/MM calculations were performed with the MOLCAS 7.4 package,[5] coupled with a modified version of the MM package Tinker 4.2.[6]
An electronic embedding scheme was applied, using hydrogen link atoms (HLA) with a scaled-charge model to treat the QM/MM boundary region.[7, 8]
The frontier is placed at the CO-CαH and NH–CαH bonds of V163 and L165, respectively, and at the Cα-Cβ bond of E243. The QM models **M1** and **M2** (see Scheme 1 of the main text) were employed in QM/MM calculations of VP and W164Y enzymes, respectively. Model **M1** (40 atoms) includes the tryptophan residue (W164) with the CO and NH bonds of V163 and L165, respectively, and the negatively charged glutamate residue (E243). Model **M2** (37 atoms) is comprised of the tyrosyl residue (Y164) with the CO and NH bonds of V163 and L165, respectively, and the glutamate residue (E243). In both cases the overall charge for the QM part is -1 for the non-radical species and 0 for the radical species.
To correctly describe the frontier the HLA may interact with all the MM point charges, but cannot be involved in other MM potentials. The charges of the frontier MM carbon atoms were set to 0 to ensure that the QM wavefunction is not overpolarized by the proximity of HLA atoms. This procedure is allowed by the small values of the original CHARMM27 point charges.

Table S1. Partial charges used for V163, L165 and E243 at the frontier region.

Residue	**Charge**					
	Cα	**Hα**	**N**	**H**	**C**	**O**
V163	0.0000	0.0000	-0.3740	0.3740	-	-
L165	0.0000	0.0000	-	-	0.5100	-0.5100
E243	0.0000	0.0000	-0.4284	0.3388	0.5548	-0.4652

Both subsystems (QM and MM) interact in the following way: (a) the QM wave function is polarized by all the MM point charges; (b) stretching, bending and torsion potentials involving at least one MM atom are described at the MM level; (c) standard van der Waals potentials are used to represent the interaction between atom pairs (QM/MM) separated by more than two bonds.
Therefore, the Hamiltonian used in the computations takes the following form:

$$\hat{H} = \hat{H}_{QM} + \hat{H}_{MM} + \sum_{i=1}^{n}\sum_{j=1}^{Q} -\frac{q_j}{r_{ij}} + \sum_{i=1}^{N}\sum_{j=1}^{Q} \frac{Z_i q_j}{r_{ij}} + E_{vdW} + E_{bonded}$$

where $\hat{H}_{QM}$ is the Hamiltonian of the QM subsystem *in vacuo*. $\hat{H}_{MM}$ is the Hamiltonian of the MM subsystem computed using the CHARMM27 forcefield, and the remaining four terms are the interacting QM/MM Hamiltonian. The first two terms comprise the electrostatic interactions (polarization of the wavefunction by the MM charges and Coulomb term between QM and MM nuclei) that were approximated using the ElectroStatic Potential Fitted method (ESPF) implemented in MOLCAS. The third term corresponds to the van der Waals interaction term computed using the definition of the CHARMM27 forcefield, and the last one contains the terms needed for a proper description of the frontier within the hydrogen link atom scheme. The active MM region has been defined to include all residues and solvent molecules that have atoms within a distance of 5 Å around any QM atoms and R257, K253 and S246 residues.
Here we explicitly specify the protein residues belonging to the chosen active region: P159, V160, E161, V162, V163, W164/Y164, L165, L166, A167, S168, F193, F198, Q239, T240, A241, E243, Q245, S246, M247, V248, N250, Q251, P252, K253, I254, Q255, N256, R257, F258, A259, A260, T261, M262.

2. Results

2.1 EPR magnetic parameters

The theoretical framework for present day EPR calculations is provided by hybrid DFT methods,[9-17] that give better results than those delivered by the "pure" functionals or by competing theories based on correlated *ab initio* methods.[18] Among hybrid functionals, B3LYP[19-21] gives good theoretical results for EPR spectroscopy. Viable alternatives are PBE0[9] and TPSSh.[22] For the calculations of EPR properties a predefined special basis set can be used, such as the polarized triple-ζ valence basis set TZVP or the Barone's[23, 24] EPR-II basis set. The spectroscopic data were obtained from additional single-point calculations at all sets of optimized structures using several hybrid density functionals (B3LYP, PBE0, TPSSh) in combination with the TZVP and EPR-II spectroscopic basis set for all atoms (see Table S2-16). These calculations were performed with the program package ORCA.[25]
For B3LYP/TZVP computed values and abbreviations see the main paper.

Table S2. g-tensors, hfcc (mT) and Mulliken spin densities computed for **VP_10ns-neu** structure.

		B3LYP/EPR-II	PBE0/EPR-II	PBE0/TZVP	TPSSh/EPR-II	TPSSh/TZVP
g-tensors						
g_i	**iso**	2.00280	2.00279	2.00285	2.00277	2.00283
	x	2.00341	2.00341	2.00350	2.00333	2.00343
	y	2.00268	2.00266	2.00274	2.00266	2.00274
	z	2.00231	2.00230	2.00232	2.00232	2.00233
hfcc						
A_i(H-β1)	**iso**	2.77	2.72	2.58	2.85	2.71
	x	2.65	2.60	2.45	2.74	2.60
	y	2.95	2.90	2.76	3.03	2.90
	z	2.71	2.66	2.51	2.79	2.65
A_i(H-β2)	**iso**	1.07	1.06	1.01	1.09	1.05
	x	1.02	1.00	0.95	1.03	0.93
	y	0.96	0.94	0.90	0.97	0.98
	z	1.24	1.23	1.19	1.26	1.22
A_i(H1)	**iso**	-0.08	-0.06	-0.06	-0.08	-0.06
	x	-0.23	-0.22	-0.22	-0.23	-0.21
	y	0.19	0.20	0.20	0.18	0.20
	z	-0.19	-0.17	-0.17	-0.18	-0.16
A_i(H2)	**iso**	-0.20	-0.19	-0.19	-0.24	-0.23
	x	-0.35	-0.34	-0.33	-0.38	-0.37
	y	0.06	0.07	0.07	0.02	0.03
	z	-0.32	-0.31	-0.30	-0.36	-0.34
A_i(H-5)	**iso**	-0.53	-0.51	-0.58	-0.58	-0.59
	x	-0.78	-0.75	-0.82	-0.83	-0.83
	y	-0.23	-0.22	-0.28	-0.27	-0.29
	z	-0.59	-0.57	-0.62	-0.64	-0.64
A_i(H-7)	**iso**	-0.44	-0.42	-0.47	-0.47	-0.47
	x	-0.15	-0.14	-0.19	-0.18	-0.19
	y	-0.69	-0.66	-0.73	-0.73	-0.72
	z	-0.47	-0.45	-0.50	-0.51	-0.51
A_i(N1)	**iso**	0.26	0.23	0.23	0.20	0.17
	x	-0.04	-0.08	-0.08	-0.10	-0.14
	y	-0.06	-0.09	-0.10	-0.12	-0.16
	z	0.89	0.88	0.87	0.83	0.80
spin densities						
N1		0.19	0.19	0.20	0.19	0.19
C2		0.03	0.01	-0.01	0.02	-0.02
C3		0.49	0.56	0.61	0.52	0.60
C5		0.22	0.26	0.28	0.23	0.27
C6		-0.07	-0.09	-0.12	-0.08	-0.11
C7		0.17	0.19	0.20	0.18	0.19
C8		0.02	0.01	0.01	0.02	0.03

Table S3. g-tensors, hfcc (mT) and Mulliken spin densities computed for **VP_9.8ns-neu** structure.

		B3LYP/EPR-II	PBE0/EPR-II	PBE0/TZVP	TPSSh/EPR-II	TPSSh/TZVP
g-tensors						
g_i	**iso**	2.00280	2.00279	2.00285	2.00277	2.00283
	x	2.00342	2.00342	2.00351	2.00333	2.00344
	y	2.00268	2.00265	2.00273	2.00266	2.00273
	z	2.00231	2.00230	2.00231	2.00232	2.00233
hfcc						
A_i(H-β1)	**iso**	2.77	2.72	2.58	2.85	2.71
	x	2.65	2.66	2.45	2.74	2.60
	y	2.95	2.90	2.77	3.03	2.90
	z	2.71	2.60	2.52	2.79	2.65
A_i(H-β2)	**iso**	1.01	1.00	0.96	1.02	0.98
	x	0.96	0.94	0.89	0.97	0.92
	y	0.90	0.88	0.84	0.91	0.87
	z	1.18	1.17	1.13	1.19	1.16
A_i(H1)	**iso**	-0.06	-0.06	-0.05	-0.06	-0.04
	x	-0.21	-0.20	-0.19	-0.20	-0.18
	y	0.19	0.19	0.20	0.17	0.19
	z	-0.17	-0.16	-0.15	-0.17	-0.14
A_i(H2)	**iso**	-0.21	-0.21	-0.20	-0.25	-0.23
	x	-0.35	-0.36	-0.34	-0.39	-0.38
	y	0.06	0.06	0.07	0.01	0.03
	z	-0.32	-0.32	-0.31	-0.36	-0.35
A_i(H-5)	**iso**	-0.53	-0.58	-0.57	-0.57	-0.58
	x	-0.76	-0.82	-0.81	-0.82	-0.82
	y	-0.23	-0.28	-0.28	-0.27	-0.29
	z	-0.58	-0.63	-0.61	-0.63	-0.63
A_i(H-7)	**iso**	-0.44	-0.49	-0.48	-0.48	-0.48
	x	-0.15	-0.19	-0.19	-0.18	-0.19
	y	-0.70	-0.76	-0.74	-0.74	-0.74
	z	-0.48	-0.52	-0.50	-0.52	-0.51
A_i(N1)	**iso**	0.27	0.26	0.23	0.21	0.17
	x	-0.04	-0.05	-0.08	-0.10	-0.14
	y	-0.05	-0.06	-0.10	-0.11	-0.15
	z	0.90	0.89	0.87	0.83	0.81
spin densities						
N1		0.19	0.19	0.20	0.19	0.19
C2		0.03	0.02	-0.01	0.02	-0.01
C3		0.49	0.53	0.61	0.52	0.60
C5		0.21	0.23	0.28	0.23	0.27
C6		-0.07	-0.09	-0.12	-0.08	-0.11
C7		0.17	0.19	0.21	0.18	0.20
C8		0.02	0.01	0.01	0.02	0.02

Table S4. g-tensors, hfcc (mT) and Mulliken spin densities computed for **VP_9.6ns-neu** structure.

		B3LYP/EPR-II	PBE0/EPR-II	PBE0/TZVP	TPSSh/EPR-II	TPSSh/TZVP
g-tensors						
g_i	**iso**	2.00279	2.00278	2.00285	2.00277	2.00284
	x	2.00341	2.00340	2.00352	2.00333	2.00346
	y	2.00266	2.00263	2.00272	2.00265	2.00273
	z	2.00231	2.00230	2.00231	2.00233	2.00233
hfcc						
A_i(H-β1)	**iso**	2.79	2.73	2.59	2.86	2.73
	x	2.67	2.61	2.47	2.75	2.61
	y	2.97	2.91	2.78	3.04	2.91
	z	2.73	2.67	2.53	2.80	2.66
A_i(H-β2)	**iso**	0.96	0.95	0.91	0.97	0.93
	x	0.91	0.90	0.85	0.92	0.87
	y	0.85	0.84	0.80	0.86	0.82
	z	1.13	1.12	1.08	1.14	1.10
A_i(H1)	**iso**	-0.09	-0.09	-0.07	-0.09	-0.07
	x	-0.25	-0.24	-0.23	-0.24	-0.22
	y	0.17	0.17	0.18	0.15	0.18
	z	-0.20	-0.19	-0.17	-0.19	-0.17
A_i(H2)	**iso**	-0.23	-0.24	-0.23	-0.27	-0.26
	x	-0.40	-0.40	-0.39	-0.43	-0.42
	y	0.05	0.04	0.05	0.01	0.01
	z	-0.35	-0.35	-0.34	-0.39	-0.38
A_i(H-5)	**iso**	-0.53	-0.58	-0.57	-0.58	-0.59
	x	-0.77	-0.83	-0.82	-0.83	-0.83
	y	-0.23	-0.28	-0.28	-0.27	-0.29
	z	-0.59	-0.63	-0.62	-0.64	-0.64
A_i(H-7)	**iso**	-0.43	-0.48	-0.46	-0.46	-0.46
	x	-0.15	-0.19	-0.18	-0.17	-0.18
	y	-0.68	-0.74	-0.72	-0.72	-0.71
	z	-0.46	-0.51	-0.49	-0.50	-0.50
A_i(N1)	**iso**	0.26	0.25	0.23	0.20	0.17
	x	-0.04	-0.05	-0.08	-0.10	-0.13
	y	-0.05	-0.06	-0.09	-0.11	-0.15
	z	0.88	0.87	0.85	0.81	0.79
spin densities						
N1		0.19	0.19	0.19	0.18	0.19
C2		0.04	0.03	0.01	0.03	0.00
C3		0.49	0.52	0.60	0.51	0.59
C5		0.21	0.23	0.28	0.23	0.27
C6		-0.07	-0.09	-0.12	-0.08	-0.10
C7		0.17	0.18	0.20	0.18	0.19
C8		0.02	0.01	0.01	0.02	0.03

Table S5. g-tensors, hfcc (mT) and Mulliken spin densities computed for **VP_9.4ns-neu** structure.

		B3LYP/EPR-II	PBE0/EPR-II	PBE0/TZVP	TPSSh/EPR-II	TPSSh/TZVP
g-tensors						
g_i	**iso**	2.00280	2.00279	2.00285	2.00276	2.00282
	x	2.00342	2.00342	2.00350	2.00332	2.00342
	y	2.00268	2.00266	2.00274	2.00266	2.00273
	z	2.00231	2.00230	2.00232	2.00231	2.00233
hfcc						
A_i(H-β1)	**iso**	2.78	2.73	2.59	2.87	2.73
	x	2.66	2.61	2.46	2.76	2.61
	y	2.96	2.91	2.78	3.05	2.92
	z	2.72	2.67	2.53	2.81	2.67
A_i(H-β2)	**iso**	1.03	1.01	0.97	1.04	1.00
	x	0.97	0.96	0.91	0.99	0.94
	y	0.92	0.90	0.86	0.93	0.89
	z	1.20	1.18	1.15	1.21	1.17
A_i(H1)	**iso**	-0.06	-0.06	-0.05	-0.06	-0.04
	x	-0.20	-0.20	-0.19	-0.20	-0.18
	y	0.18	0.19	0.20	0.17	0.19
	z	-0.16	-0.16	-0.15	-0.16	-0.14
A_i(H2)	**iso**	-0.18	-0.18	-0.17	-0.22	-0.21
	x	-0.32	-0.32	-0.31	-0.36	-0.34
	y	0.07	0.07	0.08	0.03	0.04
	z	-0.30	-0.30	-0.29	-0.34	-0.33
A_i(H-5)	**iso**	-0.53	-0.58	-0.57	-0.58	-0.59
	x	-0.78	-0.84	-0.82	-0.84	-0.84
	y	-0.23	-0.28	-0.28	-0.27	-0.29
	z	-0.59	-0.64	-0.62	-0.64	-0.64
A_i(H-7)	**iso**	-0.44	-0.48	-0.47	-0.47	-0.47
	x	-0.15	-0.19	-0.19	-0.18	-0.19
	y	-0.68	-0.74	-0.73	-0.73	-0.73
	z	-0.47	-0.51	-0.50	-0.51	-0.51
A_i(N1)	**iso**	0.28	0.27	0.24	0.21	0.18
	x	-0.04	-0.05	-0.10	-0.10	-0.14
	y	-0.05	-0.06	-0.08	-0.11	-0.16
	z	0.92	0.92	0.90	0.86	0.83
spin densities						
N1		0.20	0.20	0.20	0.20	0.20
C2		0.02	0.01	-0.02	0.01	-0.03
C3		0.50	0.53	0.61	0.52	0.60
C5		0.22	0.23	0.28	0.23	0.27
C6		-0.07	-0.09	-0.12	-0.08	-0.10
C7		0.17	0.18	0.20	0.18	0.19
C8		0.02	0.01	0.01	0.02	0.03

Table S6. g-tensors, hfcc (mT) and Mulliken spin densities computed for **VP_9.2ns-neu** structure.

		B3LYP/EPR-II	PBE0/EPR-II	PBE0/TZVP	TPSSh/EPR-II	TPSSh/TZVP
g-tensors						
g_i	**iso**	2.00280	2.00279	2.00285	2.00277	2.00283
	x	2.00342	2.00341	2.00349	2.00334	2.00344
	y	2.00267	2.00264	2.00272	2.00265	2.00272
	z	2.00231	2.00230	2.00232	2.00233	2.00234
hfcc						
A_i(H-β1)	**iso**	2.84	2.78	2.64	2.92	2.78
	x	2.72	2.66	2.51	2.81	2.66
	y	3.02	2.97	2.83	3.10	2.96
	z	2.78	2.73	2.58	2.86	2.71
A_i(H-β2)	**iso**	0.99	0.98	0.94	1.00	0.96
	x	0.94	0.92	0.88	0.95	0.90
	y	0.88	0.87	0.83	0.89	0.85
	z	1.16	1.15	1.12	1.17	1.14
A_i(H1)	**iso**	-0.07	-0.07	-0.06	-0.07	-0.05
	x	-0.22	-0.22	-0.21	-0.22	-0.20
	y	0.18	0.18	0.20	0.17	0.19
	z	-0.18	-0.17	-0.16	-0.18	-0.15
A_i(H2)	**iso**	-0.22	-0.22	-0.21	-0.26	-0.25
	x	-0.37	-0.37	-0.36	-0.41	-0.40
	y	0.06	0.05	0.06	0.01	0.02
	z	-0.33	-0.33	-0.32	-0.38	-0.36
A_i(H-5)	**iso**	-0.53	-0.58	-0.57	-0.57	-0.58
	x	-0.76	-0.83	-0.81	-0.82	-0.82
	y	-0.23	-0.28	-0.28	-0.27	-0.28
	z	-0.58	-0.63	-0.61	-0.63	-0.63
A_i(H-7)	**iso**	-0.45	-0.50	-0.48	-0.48	-0.49
	x	-0.15	-0.19	-0.19	-0.18	-0.19
	y	-0.70	-0.77	-0.75	-0.75	-0.74
	z	-0.48	-0.52	-0.51	-0.52	-0.52
A_i(N1)	**iso**	0.26	0.25	0.22	0.20	0.16
	x	-0.04	-0.05	-0.08	-0.10	-0.14
	y	-0.06	-0.07	-0.10	-0.12	0.16
	z	0.87	0.87	0.85	0.81	0.79
spin densities						
N1		0.19	0.19	0.19	0.19	0.19
C2		0.03	0.02	0.01	0.02	-0.01
C3		0.49	0.53	0.60	0.52	0.59
C5		0.21	0.23	0.28	0.23	0.27
C6		-0.07	-0.09	-0.12	-0.08	-0.11
C7		0.18	0.19	0.21	0.18	0.20
C8		0.01	-0.01	-0.01	0.01	0.02

Table S7. g-tensors, hfcc (mT) and Mulliken spin densities computed for **VP_10ns-cat** structure.

		B3LYP/EPR-II	PBE0/EPR-II	PBE0/TZVP	TPSSh/EPR-II	TPSSh/TZVP
g-tensors						
g_i	**iso**	2.00278	2.00275	2.00283	2.00283	2.00290
	x	2.00339	2.00337	2.00346	2.00338	2.00350
	y	2.00261	2.00256	2.00269	2.00271	2.00279
	z	2.00235	2.00233	2.00235	2.00239	2.00241
hfcc						
A_i(H-β1)	**iso**	2.49	2.45	2.32	2.54	2.42
	x	2.38	2.34	2.21	2.44	2.32
	y	2.65	2.62	2.50	2.70	2.59
	z	2.43	2.39	2.27	2.48	2.36
A_i(H-β2)	**iso**	0.94	0.93	0.89	0.94	0.91
	x	0.89	0.99	0.84	0.90	0.86
	y	0.83	0.82	0.79	0.83	0.80
	z	1.09	1.08	1.05	1.09	1.06
A_i(H1)	**iso**	-0.38	-0.37	-0.36	-0.36	-0.34
	x	-0.67	-0.67	-0.66	-0.65	-0.63
	y	0.06	0.06	0.07	0.06	0.07
	z	-0.51	-0.50	-0.49	-0.49	-0.47
A_i(H2)	**iso**	-0.35	-0.38	-0.36	-0.39	-0.38
	x	-0.46	-0.48	-0.46	-0.50	-0.48
	y	-0.01	-0.03	-0.02	-0.06	-0.05
	z	-0.58	-0.61	-0.59	-0.61	-0.59
A_i(H-5)	**iso**	-0.57	-0.62	-0.62	-0.62	-0.63
	x	-0.84	-0.91	-0.89	-0.90	-0.90
	y	-0.24	-0.29	-0.29	-0.28	-0.30
	z	-0.63	-0.68	-0.66	-0.68	-0.68
A_i(H-7)	**iso**	-0.46	-0.51	-0.49	-0.49	-0.49
	x	-0.15	-0.20	-0.19	-0.18	-0.19
	y	-0.72	-0.78	-0.76	-0.76	-0.75
	z	-0.50	-0.54	-0.52	-0.53	-0.53
A_i(N1)	**iso**	0.21	0.20	0.18	0.17	0.14
	x	-0.05	-0.06	-0.08	-0.09	-0.13
	y	-0.07	-0.07	-0.10	-0.11	-0.14
	z	0.75	0.74	0.73	0.70	0.68
spin densities						
N1		0.16	0.15	0.15	0.15	0.15
C2		0.10	0.10	0.08	0.09	0.06
C3		0.42	0.46	0.53	0.45	0.52
C5		0.23	0.25	0.29	0.24	0.29
C6		-0.08	-0.10	-0.12	-0.09	-0.11
C7		0.18	0.19	0.21	0.19	0.20
C8		0.04	0.03	0.04	0.05	0.06

Computed EPR parameters of tryptophan radicals were found almost independent of the choice of hybrid functional (B3LYP, PBE0 or TPSSh) and basis set (TZVP or EPR-II). Indeed, g-tensors and hfcc values computed for the same structure, using the six different combinations of functional and basis set displayed, vary within a maximum of 200 ppm and 0.2 mT, respectively.

Table S8. B3LYP/TZVP g-tensors, hfcc (mT) and Mulliken spin densities computed for **VP_10ns-TS**.

		g-tensors	hfcc							spin densities						
		g_i	A_i(H-β1)	A_i(H-β2)	A_i(H1)	A_i(H2)	A_i(H5)	A_i(H7)	A_i(N1)	N1	C2	C3	C5	C6	C7	C8
VP_10ns-TS	**iso**	2.00285	2.47	0.93	-0.25	-0.30	-0.54	-0.44	0.20	0.16	0.06	0.51	0.27	-0.10	0.20	0.04
	x	2.00348	2.35	0.87	-0.48	-0.41	-0.80	-0.15	-0.07							
	y	2.00273	2.65	0.82	0.12	0.01	-0.23	-0.71	-0.09							
	z	2.00234	2.41	1.09	-0.38	-0.50	-0.59	-0.48	0.77							

Table S9. B3LYP/TZVP g-tensors, hfcc (mT) and Mulliken spin densities computed for the QM/MM optimized geometry of a neutral tryptophan radical not H-bonded (**VP_10ns-neu-B**), obtained after breaking the N1-H1 hydrogen bond with E243 and allowing E243 residue to form a hydrogen bond with a nearby water molecule after rotation around the C-O2 bond.

		g-tensors	hfcc							spin densities						
		g_i	A_i(H-β1)	A_i(H-β2)	A_i(H1)	A_i(H2)	A_i(H5)	A_i(H7)	A_i(N1)	N1	C2	C3	C5	C6	C7	C8
VP_10ns-neu-B	**iso**	2.00296	2.85	1.02	0.00	-0.03	-0.47	-0.38	0.28	0.25	-0.08	0.61	0.24	-0.08	0.17	0.01
	x	2.00376	2.71	0.95	-0.02	-0.09	-0.67	-0.12	-0.11							
	y	2.00284	3.05	0.91	0.04	0.16	-0.21	-0.61	-0.12							
	z	2.00227	2.78	1.21	-0.01	-0.15	-0.52	-0.41	1.06							

Table S10. g-tensors, hfcc (mT) and Mulliken spin densities computed for **W164Y_10ns-B** structure.

		B3LYP/EPR-II	PBE0/EPR-II	PBE0/TZVP	TPSSh/EPR-II	TPSSh/TZVP
g-tensors						
g_i	**iso**	2.0052	2.0053	2.0053	2.0048	2.0049
	x	2.0087	2.0087	2.0090	2.0078	2.0079
	y	2.0047	2.0048	2.0047	2.0045	2.0045
	z	2.0023	2.0023	2.0023	2.0023	2.0023
hfcc						
A_i(H-β1)	**iso**	2.50	2.43	2.29	2.58	2.45
	x	2.63	2.57	2.43	2.72	2.59
	y	2.39	2.32	2.17	2.49	2.34
	z	2.46	2.40	2.26	2.55	2.41
A_i(H-β2)	**iso**	0.64	0.63	0.60	0.66	0.63
	x	0.58	0.57	0.54	0.60	0.57
	y	0.78	0.77	0.75	0.80	0.77
	z	0.56	0.55	0.53	0.57	0.55
A_i(H2)	**iso**	0.21	0.29	0.29	0.21	0.23
	x	0.19	0.24	0.25	0.18	0.20
	y	0.33	0.43	0.44	0.35	0.36
	z	0.11	0.18	0.18	0.11	0.13
A_i(H6)	**iso**	0.21	0.29	0.29	0.22	0.23
	x	0.20	0.25	0.26	0.19	0.21
	y	0.34	0.44	0.45	0.35	0.37
	z	0.11	0.18	0.18	0.12	0.12
A_i(H3)	**iso**	-0.63	-0.71	-0.69	-0.68	-0.68
	x	-0.94	-1.04	-1.02	-1.00	-0.99
	y	-0.24	-0.30	-0.30	-0.28	-0.29
	z	-0.71	-0.78	-0.76	-0.77	-0.76
A_i(H5)	**iso**	-0.65	-0.73	-0.71	-0.71	-0.72
	x	-0.96	-1.06	-1.04	-1.04	-1.03
	y	-0.25	-0.31	-0.31	-0.30	-0.32
	z	-0.74	-0.81	-0.79	-0.80	-0.80
spin densities						
C1		0.38	0.46	0.46	0.41	0.45
C2		-0.12	-0.15	-0.18	-0.14	-0.17
C3		0.25	0.31	0.31	0.27	0.30
C4		-0.01	-0.03	-0.05	-0.01	-0.03
C5		0.26	0.31	0.31	0.27	0.30
C6		-0.12	-0.15	-0.18	-0.14	-0.17
O1		0.35	0.36	0.36	0.35	0.35

Table S11. g-tensors, hfcc (mT) and Mulliken spin densities computed for **W164Y_9.8ns-B** structure.

		B3LYP/EPR-II	PBE0/EPR-II	PBE0/TZVP	TPSSh/EPR-II	TPSSh/TZVP
g-tensors						
g_i	**iso**	2.0051	2.0051	2.0052	2.0047	2.0048
	x	2.0083	2.0083	2.0086	2.0074	2.0076
	y	2.0047	2.0048	2.0047	2.0045	2.0045
	z	2.0023	2.0023	2.0023	2.0023	2.0023
hfcc						
A_i(H-β1)	**iso**	2.46	2.40	2.26	2.55	2.41
	x	2.60	2.54	2.40	2.68	2.55
	y	2.35	2.29	2.14	2.45	2.31
	z	2.43	2.37	2.23	2.52	2.38
A_i(H-β2)	**iso**	0.67	0.66	0.63	0.69	0.66
	x	0.61	0.60	0.57	0.63	0.60
	y	0.82	0.80	0.78	0.83	0.80
	z	0.59	0.58	0.55	0.60	0.58
A_i(H2)	**iso**	0.20	0.27	0.28	0.20	0.22
	x	0.18	0.23	0.24	0.18	0.19
	y	0.32	0.42	0.42	0.33	0.34
	z	0.10	0.17	0.17	0.10	0.11
A_i(H6)	**iso**	0.22	0.30	0.30	0.22	0.24
	x	0.20	0.25	0.26	0.19	0.21
	y	0.35	0.45	0.46	0.36	0.38
	z	0.12	0.19	0.19	0.12	0.13
A_i(H3)	**iso**	-0.61	-0.69	-0.67	-0.66	-0.66
	x	-0.91	-1.01	-0.99	-0.97	-0.96
	y	-0.23	-0.29	-0.28	-0.26	-0.27
	z	-0.69	-0.76	-0.74	-0.74	-0.74
A_i(H5)	**iso**	-0.66	-0.74	-0.72	-0.72	-0.72
	x	-0.97	-1.07	-1.05	-1.05	-1.04
	y	-0.25	-0.32	-0.31	-0.30	-0.32
	z	-0.74	-0.82	-0.80	-0.81	-0.81
spin densities						
C1		0.38	0.42	0.46	0.41	0.45
C2		-0.11	-0.14	-0.18	-0.13	-0.16
C3		0.25	0.27	0.30	0.26	0.29
C4		-0.01	-0.02	-0.05	-0.01	-0.03
C5		0.26	0.28	0.32	0.27	0.30
C6		-0.12	-0.16	-0.19	-0.14	-0.18
O1		0.35	0.36	0.36	0.34	0.35

Table S12. g-tensors, hfcc (mT) and Mulliken spin densities computed for **W164Y_9.6ns-B** structure.

		B3LYP/EPR-II	PBE0/EPR-II	PBE0/TZVP	TPSSh/EPR-II	TPSSh/TZVP
g-tensors						
g_i	**iso**	2.0051	2.0051	2.0052	2.0048	2.0048
	x	2.0085	2.0083	2.0086	2.0076	2.0078
	y	2.0047	2.0046	2.0047	2.0045	2.0044
	z	2.0023	2.0023	2.0023	2.0023	2.0023
hfcc						
A_i(H-β1)	**iso**	2.44	2.49	2.34	2.53	2.39
	x	2.58	2.63	2.49	2.66	2.53
	y	2.33	2.38	2.23	2.43	2.29
	z	2.41	2.47	2.32	2.49	2.36
A_i(H-β2)	**iso**	0.65	0.60	0.57	0.66	0.64
	x	0.59	0.53	0.50	0.60	0.57
	y	0.79	0.74	0.71	0.80	0.78
	z	0.57	0.52	0.49	0.58	0.56
A_i(H2)	**iso**	0.20	0.27	0.27	0.21	0.22
	x	0.18	0.23	0.24	0.18	0.20
	y	0.32	0.41	0.41	0.33	0.35
	z	0.10	0.17	0.16	0.11	0.11
A_i(H6)	**iso**	0.22	0.29	0.29	0.22	0.24
	x	0.20	0.25	0.25	0.19	0.21
	y	0.35	0.44	0.44	0.36	0.37
	z	0.12	0.17	0.17	0.12	0.13
A_i(H3)	**iso**	-0.62	-0.70	-0.68	-0.67	-0.67
	x	-0.92	-1.03	-1.00	-0.98	-0.98
	y	-0.23	-0.29	-0.28	-0.27	-0.28
	z	-0.70	-0.77	-0.75	-0.75	-0.74
A_i(H5)	**iso**	-0.66	-0.71	-0.69	-0.72	-0.73
	x	-0.98	-1.04	-1.01	-1.06	-1.05
	y	-0.25	-0.31	-0.30	-0.30	-0.32
	z	-0.74	-0.79	-0.77	-0.81	-0.81
spin densities						
C1		0.38	0.42	0.46	0.41	0.45
C2		-0.11	-0.15	-0.18	-0.13	-0.17
C3		0.25	0.28	0.30	0.26	0.29
C4		-0.01	-0.02	-0.05	-0.01	-0.03
C5		0.26	0.27	0.30	0.27	0.30
C6		-0.12	-0.16	-0.19	-0.14	-0.18
O1		0.34	0.35	0.36	0.34	0.35

Table S13. g-tensors, hfcc (mT) and Mulliken spin densities computed for **W164Y_9.4ns-B** structure.

		B3LYP/EPR-II	PBE0/EPR-II	PBE0/TZVP	TPSSh/EPR-II	TPSSh/TZVP
g-tensors						
g_i	**iso**	2.0053	2.0053	2.0054	2.0049	2.0049
	x	2.0088	2.0089	2.0091	2.0079	2.0080
	y	2.0047	2.0048	2.0047	2.0045	2.0044
	z	2.0023	2.0023	2.0023	2.0023	2.0023
hfcc						
A_i(H-β1)	**iso**	2.46	2.40	2.26	2.55	2.42
	x	2.60	2.53	2.40	2.68	2.55
	y	2.35	2.29	2.14	2.45	2.31
	z	2.43	2.37	2.23	2.52	2.38
A_i(H-β2)	**iso**	0.65	0.64	0.61	0.67	0.64
	x	0.59	0.58	0.55	0.61	0.58
	y	0.80	0.78	0.76	0.81	0.78
	z	0.57	0.56	0.54	0.58	0.56
A_i(H2)	**iso**	0.21	0.29	0.29	0.22	0.23
	x	0.19	0.24	0.25	0.19	0.21
	y	0.34	0.44	0.44	0.35	0.36
	z	0.11	0.19	0.18	0.12	0.13
A_i(H6)	**iso**	0.22	0.30	0.30	0.22	0.24
	x	0.20	0.25	0.26	0.19	0.21
	y	0.35	0.45	0.45	0.36	0.37
	z	0.11	0.19	0.18	0.12	0.13
A_i(H3)	**iso**	-0.64	-0.71	-0.69	-0.69	-0.69
	x	-0.95	-1.05	-1.02	-1.01	-1.00
	y	-0.24	-0.30	-0.30	-0.28	-0.29
	z	-0.72	-0.79	-0.76	-0.77	-0.76
A_i(H5)	**iso**	-0.65	-0.73	-0.71	-0.72	-0.72
	x	-0.96	-1.06	-1.04	-1.04	-1.03
	y	-0.26	-0.32	-0.31	-0.30	-0.32
	z	-0.74	-0.81	-0.78	-0.80	-0.80
spin densities						
C1		0.38	0.42	0.46	0.41	0.45
C2		-0.12	-0.15	-0.18	-0.14	-0.17
C3		0.26	0.28	0.31	0.27	0.30
C4		-0.01	-0.03	-0.06	-0.02	-0.04
C5		0.26	0.28	0.31	0.27	0.30
C6		-0.12	-0.16	-0.19	-0.14	-0.17
O1		0.35	0.36	0.37	0.35	0.35

Table S14. g-tensors, hfcc (mT) and Mulliken spin densities computed for **W164Y_9.2ns-B** structure.

		B3LYP/EPR-II	PBE0/EPR-II	PBE0/TZVP	TPSSh/EPR-II	TPSSh/TZVP
g-tensors						
g_i	**iso**	2.0050	2.0051	2.0052	2.0047	2.0048
	x	2.0083	2.0083	2.0086	2.0075	2.0076
	y	2.0046	2.0046	2.0047	2.0044	2.0044
	z	2.0023	2.0023	2.0023	2.0023	2.0023
hfcc						
A_i(H-β1)	**iso**	2.56	2.49	2.34	2.64	2.51
	x	2.70	2.63	2.49	2.78	2.65
	y	2.45	2.38	2.23	2.54	2.40
	z	2.53	2.47	2.32	2.61	2.47
A_i(H-β2)	**iso**	0.61	0.60	0.57	0.62	0.59
	x	0.55	0.53	0.50	0.56	0.53
	y	0.75	0.74	0.71	0.76	0.74
	z	0.53	0.52	0.49	0.53	0.51
A_i(H2)	**iso**	0.20	0.27	0.27	0.20	0.22
	x	0.18	0.23	0.24	0.18	0.20
	y	0.32	0.41	0.41	0.33	0.35
	z	0.09	0.17	0.16	0.10	0.11
A_i(H6)	**iso**	0.21	0.29	0.29	0.21	0.23
	x	0.19	0.25	0.25	0.19	0.21
	y	0.34	0.44	0.44	0.35	0.37
	z	0.10	0.17	0.17	0.11	0.12
A_i(H3)	**iso**	-0.62	-0.70	-0.68	-0.67	-0.67
	x	-0.93	-1.03	-1.00	-0.99	-0.99
	y	-0.23	-0.29	-0.28	-0.27	-0.28
	z	-0.70	-0.77	-0.75	-0.76	-0.75
A_i(H5)	**iso**	-0.63	-0.71	-0.69	-0.70	-0.70
	x	-0.94	-1.04	-1.01	-1.01	-1.01
	y	-0.24	-0.31	-0.30	-0.29	-0.31
	z	-0.72	-0.79	-0.91	-0.79	-0.78
spin densities						
C1		0.38	0.42	0.46	0.41	0.45
C2		-0.11	-0.15	-0.18	-0.13	-0.17
C3		0.25	0.28	0.30	0.27	0.29
C4		-0.01	-0.02	-0.04	-0.01	-0.03
C5		0.25	0.27	0.30	0.26	0.29
C6		-0.12	-0.15	-0.19	-0.14	-0.17
O1		0.34	0.35	0.36	0.34	0.35

Table S15. g-tensors, hfcc (mT) and Mulliken spin densities computed for **W164Y_10ns-A** structure.

		B3LYP/EPR-II	PBE0/EPR-II	PBE0/TZVP	TPSSh/EPR-II	TPSSh/TZVP
g-tensors						
g_i	**iso**	2.0044	2.0044	2.0045	2.0042	2.0043
	x	2.0064	2.0064	2.0067	2.0060	2.0062
	y	2.0045	2.0045	2.0046	2.0045	2.0045
	z	2.0023	2.0023	2.0023	2.0023	2.0023
hfcc						
A_i(H-β1)	**iso**	2.73	2.65	2.50	2.78	2.64
	x	2.87	2.80	2.65	2.92	2.79
	y	2.61	2.54	2.37	2.68	2.53
	z	2.69	2.62	2.46	2.75	2.60
A_i(H-β2)	**iso**	0.63	0.62	0.59	0.62	0.60
	x	0.57	0.55	0.52	0.56	0.54
	y	0.77	0.76	0.74	0.77	0.75
	z	0.54	0.53	0.51	0.54	0.52
A_i(H2)	**iso**	0.16	0.23	0.23	0.16	0.18
	x	0.14	0.20	0.20	0.14	0.15
	y	0.28	0.36	0.37	0.29	0.30
	z	0.06	0.12	0.12	0.06	0.07
A_i(H6)	**iso**	0.17	0.24	0.25	0.17	0.19
	x	0.16	0.21	0.22	0.15	0.17
	y	0.29	0.38	0.39	0.30	0.32
	z	0.07	0.14	0.14	0.07	0.08
A_i(H3)	**iso**	-0.54	-0.61	-0.59	-0.58	-0.58
	x	-0.81	-0.90	-0.88	-0.86	-0.85
	y	-0.18	-0.23	-0.23	-0.22	-0.23
	z	-0.63	-0.69	-0.67	-0.67	-0.66
A_i(H5)	**iso**	-0.61	-0.69	-0.67	-0.68	-0.68
	x	-0.92	-1.01	-0.99	-1.00	-0.99
	y	-0.22	-0.28	-0.27	-0.27	-0.29
	z	-0.70	-0.77	-0.75	-0.77	-0.77
spin densities						
C1		0.39	0.43	0.46	0.42	0.45
C2		-0.09	-0.13	-0.15	-0.11	-0.14
C3		0.21	0.23	0.25	0.22	0.24
C4		0.04	0.03	0.02	0.04	0.03
C5		0.24	0.26	0.29	0.25	0.28
C6		-0.10	-0.14	-0.17	-0.12	-0.16
O1		0.31	0.32	0.32	0.31	0.31

The B3LYP and PBE0 EPR parameters, computed for the same structures of tyrosyl radicals, resulted to vary more than in the case of tryptophan radicals (e.g., g-tensors range within 300 ppm). The TPSSh functional provided computed g_x values about 1000 ppm lower than those computed using the other functionals. In any case, hfcc values computed for tyrosyl radicals vary within 0.3 mT.

Table S16. B3LYP/TZVP g-tensors, hfcc (mT) and Mulliken spin densities computed for a QM/MM optimized structure of tyrosyl radical (**W164Y_10ns-B2**) obtained from the optimized **W164Y_10ns-B** model, following a subsequent QM/MM optimization in which R257 side chain were included in the QM region (see also Table S18).

	g-tensors	**hfcc**						**spin densities**						
	g_i	**A_i(H-β1)**	**A_i(H-β2)**	**A_i(H2)**	**A_i(H6)**	**A_i(H3)**	**A_i(H5)**	**C1**	**C2**	**C3**	**C4**	**C5**	**C6**	**O1**
iso	2.0053	2.29	0.62	0.21	0.21	-0.61	-0.62	0.42	-0.15	0.28	-0.03	0.28	-0.15	0.36
x	2.0089	2.44	0.55	0.20	0.20	-0.92	-0.92							
y	2.0047	2.18	0.76	0.33	0.33	-0.23	-0.23							
z	2.0023	2.26	0.54	0.10	0.10	-0.69	-0.70							

Computed EPR parameters for **W164Y_10ns-B** and **W164Y_10ns-B2** models are very similar (see Table 4 in the main paper). Accordingly, the comparison of geometrical parameters shown in the following Table S18 with data in Table 6 of the main paper for the **W164Y_10ns-B** model indicates that the inclusion of R257 side chain in the QM region, which has a high computational cost, does not affect the QM/MM optimized geometry. In particular, the distance between the O1 tyrosyl oxygen and the hydrogen of the closest -NH_2 group of R257 is almost invariant between the two structures.

2.2 Optimized Structures

Table S17. Selected geometrical parameters[a] for B3LYP/CHARMM optimized geometries of VP neutral tryptophan radical.

System	**ϕ**	**N1-H1**	**N1-C2**	**N1-C9**	**C2-C3**	**C3-C4**	**C4-C5**	**C4-C9**	**C5-C6**	**C6-C7**	**C7-C8**	**C8-C9**	**H1-O2**	**θ_1**[b]	**θ_2**[b]	**ρ_{C3}**[b]
VP_9.8ns-neu	-22.960	1.531	1.322	1.420	1.456	1.427	1.406	1.422	1.398	1.397	1.414	1.382	1.071	-7.1	-52.9	0.53
VP_9.6ns-neu	-23.831	1.501	1.323	1.419	1.454	1.426	1.405	1.419	1.399	1.395	1.413	1.380	1.084	-6.0	-54.0	0.53
VP_9.4ns-neu	-23.035	1.547	1.322	1.420	1.455	1.429	1.407	1.423	1.400	1.397	1.415	1.382	1.066	-7.3	-52.7	0.53
VP_9.2ns-neu	-23.740	1.514	1.318	1.419	1.452	1.426	1.406	1.424	1.400	1.397	1.415	1.382	1.066	-6.2	-53.8	0.54
VP_10ns-neu-B	-25.950	4.049	1.317	1.419	1.448	1.432	1.399	1.425	1.402	1.396	1.414	1.383	0.994	-6.5	-53.3	0.58

[a]Distances in Å; angles in degrees. [b]Dihedral angles θ_1 and θ_2 and spin density ρ_{C3} are obtained by solving the McConnell relationships, using the program developed by Svistunenko (freely available at the URL http://privatewww.essex.ac.uk/~svist/) and providing the B3LYP/TZVP computed A_{iso}(H-β1) and A_{iso}(H-β2) values (B"=5.0 mT).

Table S18. Selected geometrical parameters[a] for the B3LYP/CHARMM optimized geometry of tyrosyl radical in **W164Y_10ns-B2** model.

System	**ϕ**	**O1-C4**	**O1-H1**	**H1-O2**	**C1-C2**	**C1-C6**	**C2-C3**	**C3-C4**	**C4-C5**	**C5-C6**	**O1--H(NH)**[b]	**O1--H(OH)**[c]	**θ_1**[d]	**θ_2**[d]	**ρ_{C1}**[d]
W164Y_10ns-B2	-29.522	1.259	3.094	0.971	1.419	1.419	1.373	1.456	1.450	1.368	2.008	4.542	-1.3	-58.7	0.40

[a]Distances in Å; angles in degrees. [b]Distance between O1 tyrosyl oxygen and the hydrogen of the closest -NH_2 group of R257. [c]H-bond distance between tyrosine O1 and the nearest water molecule. [d]Dihedral angles θ_1 and θ_2 and spin density ρ_{C1} are obtained by solving the McConnell relationships, using the program developed by Svistunenko (freely available at the URL http://privatewww.essex.ac.uk/~svist/) and providing the B3LYP/TZVP computed A_{iso}(H-β1) and A_{iso}(H-β2) values (B"=5.8 mT).

2.3 QM/MM Energies

Table S19. Absolute energies (Hartree) for DFT/CHARMM optimized structures of VP tryptophan radical (see Fig. 1).

System	B3LYP/6-31G**#	B3LYP/cc-pVTZ//B3LYP/6-31G**#	CASPT2/6-31G*//B3LYP/6-31G**#
VP_10ns-cat	-1051.30788	-1051.64834	-1048.05816
VP_10ns-TS	-1051.30425	-1051.64282	-1048.05306
VP_10ns-neu	-1051.31282	-1051.64958	-1048.06198

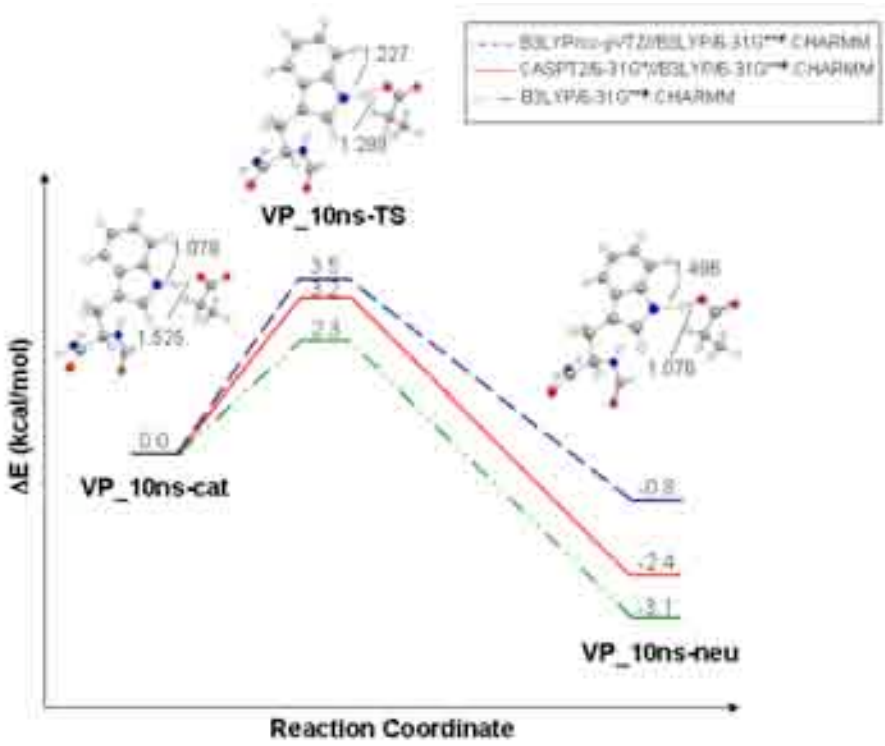

Figure S1. QM/MM energy profiles for the proton transfer in **VP_10ns** model. The relative energies (kcal/mol) of tryptophan radical cation (**VP_10ns-cat**), transition state (**VP_10ns-TS**) and neutral tryptophan radical (**VP_10ns-neu**) were computed at the B3LYP/6-31G**#:CHARMM optimized structures using different levels of theory (see inset). The N1-H1 and H1-O2 bond lengths are given in Å.

3. References

1 H. Li, A. D. Robertson, J. H. Jensen, *Proteins* 2005, **61**, 704.
2 W. Humphrey, A. Dalke, K. Schulten, *J. Molec. Graphics* 1996, **14.1**, 33.
3 A. D. MacKerell Jr., D. Bashford, M. Bellott, R. L. Dunbrack Jr., J. D. Evanseck, M. J. Field, S. Fischer, J. Gao, H. Guo, S. Ha, D. Joseph-McCarthy, L. Kuchnir, K. Kuczera, F. T. K. Lau, C. Mattos, S. Michnick, T. Ngo, D. T. Nguyen, B. Prodhom, W. E. Reiher III, B. Roux, M. Schlenkrich, J. C. Smith, R. Stote, J. Straub, M. Watanabe, J. Wiórkiewicz-Kuczera, D. Yin, M. Karplus, *J. Phys. Chem. B* 1998, **102**, 3586.
4 K. Kuczera, J. Kuriyan, M. Karplus, *J. Mol. Biol.* 1990, **213**, 351.
5 G. Karlström, R. Lindh, P.-A. Malmqvist, B. O. Roos, U. Ryde, V. Veryazov, P.-O. Widmark, M. Cossi, B. Schimmelpfennig, P. Neogrady, L. Seijo, *Comput. Mat. Sci.* 2003, **28**, 222.
6 J. W. Ponder 2004, Tinker4.2 - software tools for molecular design, Available at: http://dasher.wustl.edu/tinker
7 T. Andruniow, N. Ferré, M. Olivucci, *Proceed. Nat. Acad. Sci.* 2004, **101**, 17908–17913.
8 N. Ferré, M. Olivucci, *THEOCHEM* 2003, **632**, 71–82.
9 V. Barone, P. Cimino, *J. Chem. Theor. Comput.* 2009, **5**, 192.
10 D. A. Svistunenko, G. A. Jones, *Phys. Chem. Chem. Phys.* 2009, **11**, 6600.
11 B. Brogioni, D. Biglino, A. Sinicropi, E. Reijerse, P. Giardina, G. Sannia, W. Lubitz, R. Basosi, P. R., *Phys. Chem. Chem. Phys.* 2008, **10**, 7284.
12 M. Pavone, P. Cimino, O. Crescenzi, A. Sillanpää, V. Barone, *J. Phys. Chem. B* 2007, **111**, 8928.
13 M. van Gastel, W. Lubitz, G. Lassmann, F. Neese, *J. Am. Chem. Soc.* 2004, **126**, 2237.
14 S. Sinnecker, M. Flores, W. Lubitz, *Phys. Chem. Chem. Phys.* 2006, **8**, 5659.
15 D. Baute, D. Arieli, F. Neese, H. Zimmermann, B. M. Weckhuysen, D. Goldfarb, *J. Am. Chem. Soc.* 2004, **126**, 11733.
16 S. Un, *Magn. Res. Chem.* 2005, **43**, S229.
17 F. Neese, *J. Biol. Inorg. Chem.* 2006, **11**, 702–711.
18 F. Neese, T. Petrenko, D. Ganyushin, G. Olbrich, *Coord. Chem. Rev.* 2007, **251**, 288.
19 A. D. Becke, *J. Chem. Phys.* 1993, **98**, 5648.
20 C. Lee, W. Yang, R. G. Parr, *Phys. Rev. B* 1988, **37**, 785–789.
21 P. J. Stephens, F. J. Devlin, C. F. Chabalowski, M. J. Frisch, *J. Phys. Chem.* 1994, **98**, 11623.
22 F. Neese, *EPR Newsletter* 2009, **18**, 4.
23 V. Barone, Recent Advances in Density Functional Methods (PartI), ed. D.P. Chong ed., World Scientific Publishing Co., 1995.
24 V. Barone, A. Polimeno, *Phys. Chem. Chem. Phys.* 2006, **8**, 4609–4629.
25 F. Neese, ORCA, an ab initio, Density Functional and Semi-empirical Program Package, University of Bonn, Germany, Version 2.7, June 2009
26 B. O. Roos, in Adv. Chem. Phys. (Ab initio Methods in Quantum Chemistry-II), Vol. 69 (Ed.: K. P. Lawley), Wiley, New York, 1987, p. 399.
27 K. Andersson, P.-Å. Malmqvist, B. O. Roos, *J. Chem. Phys.* 1992, **96**, 1218– 1226.